MONTE CARLO SIMULATIONS OF GRID WALLED PROPORTIONAL COUNTERS WITH DIFFERENT SITE SIZES FOR HZE RADIATION

A Dissertation

by

HAIFENG LIU

Submitted to the Office of Graduate Studies of
Texas A&M University
in partial fulfillment of the requirements for the degree of

DOCTOR OF PHILOSOPHY

May 2012

Major Subject: Nuclear Engineering

MONTE CARLO SIMULATIONS OF GRID WALLED PROPORTIONAL

COUNTERS WITH DIFFERENT SITE SIZES

FOR HZE RADIATION

MONTE CARLO SIMULATIONS OF GRID WALLED PROPORTIONAL COUNTERS WITH DIFFERENT SITE SIZE FOR HZE RADIATION

A Dissertation

by

HAIFENG LIU

Submitted to the Office of Graduate Studies of
Texas A&M University
in partial fulfillment of the requirements for the degree of

DOCTOR OF PHILOSOPHY

Approved by:

Chair of Committee,	Leslie A. Braby
Committee Members,	W. Dan Reece
	Dudley W. Poston
	James T. White
Head of Department,	Yassin A. Hassan

May 2012

Major Subject: Nuclear Engineering

ABSTRACT

Monte Carlo Simulations of Grid Walled Proportional Counters

with Different Site Sizes for HZE Radiation. (May 2012)

Haifeng Liu, B.S.; M.S., Tsinghua University

Chair of Advisory Committee: Dr. Leslie A. Braby

Tissue-equivalent proportional counters are frequently used to measure dose and dose equivalent in cosmic radiation fields that include high-Z, high-energy (HZE) particles. The fact that particles with different stopping powers can produce the same energy deposition in the same detector means that the measure of lineal energy cannot provide enough information to evaluate the equivalent dose due to HZE particles. To characterize incident particles by mass and velocity, a multiple-detector system composed of three tissue-equivalent proportional counters simulating different size tissue volumes was proposed to be built. This system took advantage of the well-known fact that lineal energy (y) of a HZE particle depends on the site size, as well as the particle mass and energy.

Monte Carlo calculations were used to evaluate lineal energy, using GEANT4, in grid-walled (wall-less) proportional counters with simulated unit density site diameter of 0.1, 0.5 and 2.5 μm in a uniform HZE particle field. Uniform beams of 1000 MeV/n and 100 MeV/n $^{56}Fe^{26+}$, $^{28}Si^{14+}$, $^{16}O^{8+}$, $^{12}C^{6+}$, $^{4}He^{2+}$ ions and proton particles bombarding the detectors were simulated. The results of the calculations were used to determine how

much additional information about particle charge and velocity could be obtained from such a detector system. Comparison of simulation results with those of walled detectors was included in the study to illustrate the wall effect.

The results shows that the detector system is capable of characterizing HZE particles in a mixed unknown field based on the lineal energy spectra as well as the calculated mean lineal energy. This suggests that it may be practical to use such a system to measure the average particle velocity of HZE particles in space. The parameters used in the simulation are also good references for detector construction. There is only limited experimental data for lineal energy resulting from a large uniform field of HZE particles incident on a wall-less detector. However, the Monte Carlo results are consistent with the experimental data available.

ACKNOWLEDGEMENTS

I would like to thank my committee chair, Dr. Braby, and my committee members, Dr. Reece, Dr. Poston, and Dr. White, for their guidance and support throughout the course of this research.

Thanks also go to my friends and colleagues and the department faculty and staff for making my time at Texas A&M University a great experience. Finally, thanks to my mother and father for their encouragement and to my fiancée for her patience and love.

TABLE OF CONTENTS

CHAPTER Page

LIST OF FIGURES

FIGURE Page

FIGURE Page

FIGURE Page

LIST OF TABLES

CHAPTER I

INTRODUCTION

The space radiation environment includes HZE ions and their secondary particles. Many of these particles have long range and high quality factors (Q). For example, the quality factor for heavy particles can be as high as 20, while it is 1 for photons and electrons, and typically about 1.5 for protons (ICRP 1990). Although HZE particles are just a small part of the cosmic ray spectrum, characterizing them is of importance because they contribute a large portion to the total equivalent dose to astronauts. The measurement of lineal energy, instead of average quantities such as LET, can provide direct information on absorbed dose due to all types of radiation and an estimate of the effective dose, which is based on the estimate of quality factor from the relationship between the distribution of deposited energy and the distribution of LET. Tissue equivalent proportional counters, simulating tissue volumes a few micrometers in diameter, are frequently used to evaluate radiation exposures in space shuttle and space station. However, particles with different mass and velocity, indicating different quality factors, may still deposit the same amount of energy in the tissue volume. So measuring the lineal energy by single tissue equivalent proportional counters is not enough to evaluate the biological effect. In order to evaluate the effective dose, we need to characterize incident particles by charge, mass and energy.

This dissertation follows the style of *Health Physics*.

There are also instruments, such as mass spectrometers and particle telescopes, which can be used to obtain information on charge, mass and energy of the incident particle, but they are typically large and awkward and not appropriate for routine radiation dosimetry. Furthermore, they are only capable of analyzing a specific portion of the radiation spectrum. Several instruments are needed to measure the total absorbed dose. Because of the overlapping response functions of the instruments, this approach generally requires complicated data analysis to insure that the entire dose is included but none of it has been counted twice.

To improve the absorbed dose and equivalent dose measurement of HZE particles, we propose to take advantage of the size effect of lineal energy to develop a multiple detector system. The system consists of three proportional counters simulating different sized sites. For HZE particles with the same charge, mass and energy, the spectrum of lineal energy distribution f(y) in each detector will be different since a fraction of energy is carried away from the primary particle track by the secondary electrons (δ-rays), and this fraction depends on the site size. The degree of discrepancies between these spectra differs for particles with different kinetic energy and mass. We initially assumed that differences in the spectra measured by three independent detectors with different sizes will be sufficient to estimate the average velocities and mass of the incident particles.

The objective of the proposed Monte Carlo calculation of energy deposition was to provide constructive suggestions for the physical design of these detectors. What kind of detector should we use, wall-less (grid-walled) or walled detector? What simulated

site diameters should we choose? What's the measurable difference among these detectors to particles with different charge and energy? Monte Carlo simulations will help to achieve a satisfactory design for evaluating unknown radiation fields and avoid imposing unnecessarily difficult design requirements on the detectors. The Monte Carlo toolkit Geant4 is used in this simulation focusing on grid-walled detectors.

Monte-Carlo simulations of a multiple-size, solid-walled detector system have been attempted and proved the ability of the detector system to characterize radiations (Wang 2006). It is worthwhile to compare the results of two (grid-walled and solid-walled) detector systems to demonstrate their advantages and disadvantages. We can see the impact of the wall effect of solid-walled detectors on the lineal energy distribution, the frequency mean energy y_F and the size effect. The comparison also shows the practicability of both systems if they are applied to characterize the HZE particles in galactic cosmic rays.

CHAPTER II

BACKGROUND

Microdosimetry is 'the systematic study and quantification of the spatial and temporal distribution of absorbed energy in irradiated matter' (Rossi and Zaider 1996). The measurement is focused on the energy deposited in short segments of a charged particle track. Microdosimetry is most useful at low doses because the energy distribution in target sites becomes significantly different from the average due to track structure. The size of target sites relevant for microdosimetry normally varies from DNA molecules (~10 nm) to a cluster of cells (~1 mm). When site size changes, the portion of the track segment involved in measurement changes, resulting in different average of deposited energy. The size effect is critical for HZE particles, because a large portion of the energy is carried away from the primary track by δ-rays. The fraction of the energy deposited by the primary particle varies with the size.

Lineal Energy

The lineal energy, *y*, is the quotient of ε by $\bar{l}$, where ε is the energy imparted to the matter in a volume of interest by an energy deposition event, and $\bar{l}$ is the mean chord length in that volume:

$$y = \frac{\varepsilon}{\bar{l}} \tag{2.1}$$

Unit: J m^{-1}. ε may be expressed in eV and hence y may be expressed in eV/m or some convenient submultiple or multiple such as keV/μm.

The mean chord length in a convex site is

$$\bar{l} = \frac{4V}{S} \tag{2.2}$$

where V is the volume and S is the surface area of the site (Rossi and Zaider 1996). The mean chord length of a sphere is $\bar{l}$=2d/3, where d is the diameter of the sphere.

Microdosimetric Spectrum

In an irradiated site the lineal energy *y* is subject to a probability density distribution, f(*y*) (Fig. 2.1). The first moment of the probability density of *y*, which is called the frequency mean lineal energy y_F, can be calculated

$$y_F = \int y f(y)\, dy \tag{2.3}$$

But a linear representation, f(*y*) vs *y*, is not convenient to express the relationship, because f(*y*) will take values that range over 8 orders of magnitude (Rossi and Zaider 1996). The most commonly used representations of the spectra are *y*f(*y*) vs log(*y*) (Fig. 2.2).

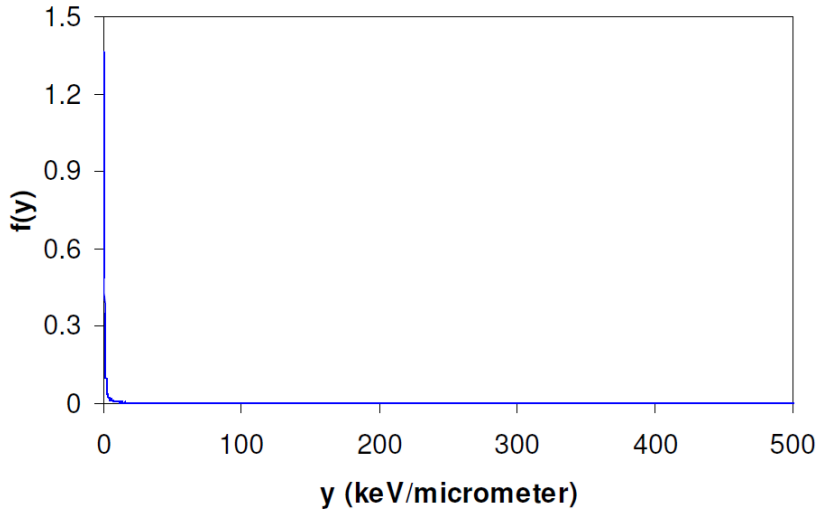

Figure 2.1 Calculated microdosimetric spectrum, f(*y*), for energy deposited by 500 MeV $^{56}Fe^{26+}$ in a 0.1 μm diameter spherical detector with 2 mm tissue equivalent wall. We can see that details of the distribution are 'hidden' by this linear representation. (Wang 2006)

Based on the fact that:

$$\int_{y_1}^{y_2} f(y)\,dy = \int_{y_1}^{y_2} \ln(10)\,[yf(y)]\,d\log(y) \tag{2.4}$$

the area delimited by any two values of *y* is proportional to the fractional number of events that have lineal energy in that range of *y* values. Thus, by displaying spectra in a semi-log representation, one is able to estimate from the plot the fraction of events that have lineal energy values in a given range of interest.

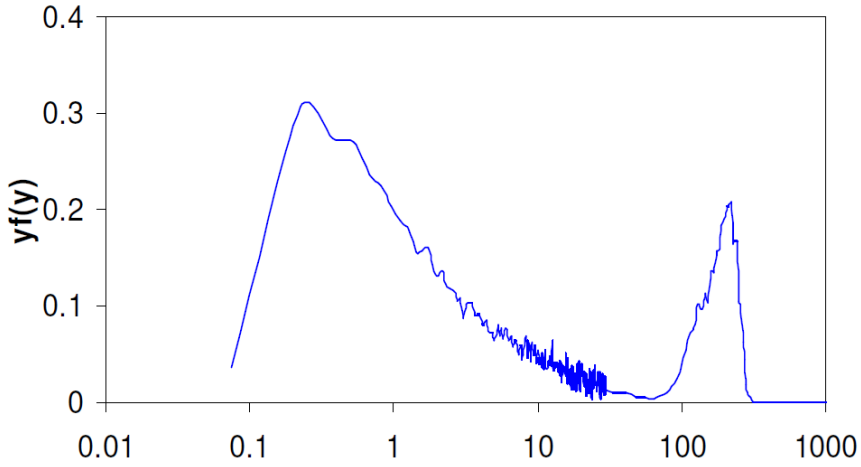

Figure 2.2. A semi-log representation of the same spectrum in Fig. 2.1. Note that the ordinate has been multiplied by *y*. The area under the curve in a range of *y* is proportional to the fraction of events in this range. (Wang 2006)

Galactic Cosmic Rays

There are three main natural sources of radiation in space to which spacecraft and astronauts may be exposed: (1) galactic cosmic rays (GCR), (2) solar particle events (SPE), and (3) trapped particles. Additional sources of radiation are the secondary protons, neutrons and ion fragmentation products produced by the interaction of energetic particles with a planetary atmosphere or surface.

Interstellar space is filled isotropically with high-energy charged particles, which are believed to be accelerated at shocks produced by supernova explosions, collectively called galactic cosmic rays (GCR). GCR is the major radiation in space outside the magnetosphere. They consist of 98 percent protons and heavier ions and two percent

electrons and positrons. Their energy spectra in free space, outside Earth's magnetic field, ranges from a few tens of MeV/n to above 1 GeV/n. Typical energy spectra for four of the most numerous and important components (protons, helium ions, oxygen ions and iron ions) are given in Fig. 2.3. The spectrum of radiation from GCR is modified by the solar wind from the sun, which carries magnetic fields that point radially away from the sun. When the solar wind is not so strong in the years of lower solar activity, the intensity of GCR is high. The cyclic activity of the sun causes a smoothly varying intensity of GCR with the lowest fluxes occurring when solar activity is highest and vice versa. The lower energy portion of the GCR energy spectrum is affected the most.

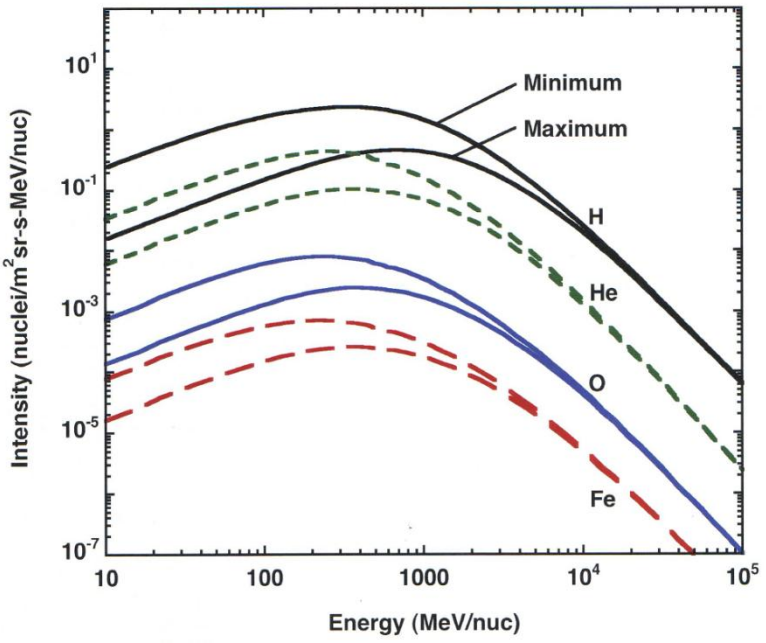

Figure 2.3. Representive GCR ion spectra depicting the intensity variations between solar maximum and minimum conditions. The upper curve for each species is for solar minimum, when cosmic rays can penetrate into inner heliosphere more easily. (Courtesy of R.A. Mewaldt, California Institute of Technology)

The fluence rate is greatest in the energy range of 100 MeV/n to 1000 MeV/n. Protons make up approximately 87 percent of the particle fluence of GCR. About 12 percent of GCR are helium ions and a small (one percent), but important component, consists of the heavier ions called high-Z and high-Energy (HZE) particles. The relative abundances of the ion species vary only slightly with energy. A compilation of relative abundances in the 2 GeV/n energy region is shown in Fig. 2.4.

Most of the dose from GCR can be accounted for by the contributions from H, He, C, O, Si and Fe. Although HZE particles are only a tiny fraction of the GCR population, their contribution to the GCR dose is substantial. Iron is the most important of the HZE particles because of its relative contribution to the GCR dose and its high linear energy transfer (Fig. 2.5).

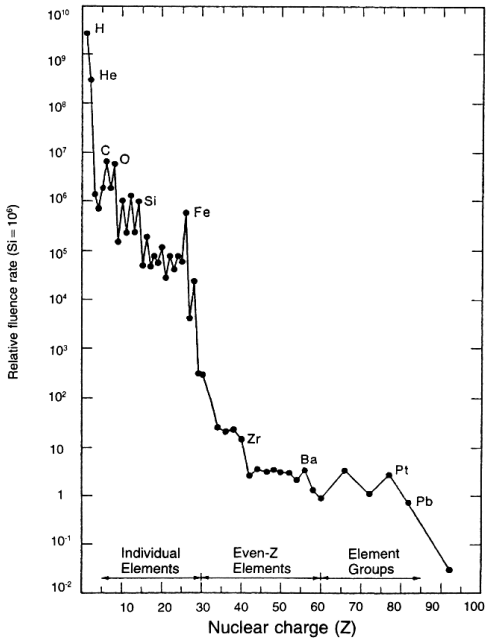

Figure 2.4. Nuclear composition of GCR (~2 GeV/n). (NCRP 1989)

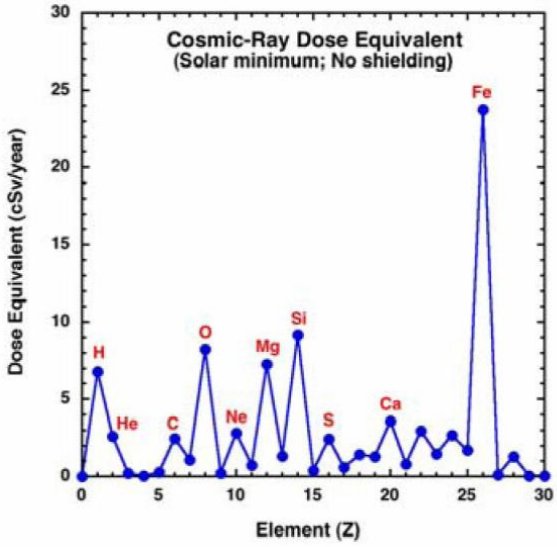

Figure 2.5. Calculated contribution to the yearly equivalent dose (in cSv/yr) due to elements from H to Ni (assuming no shielding). Note that heavy elements make the largest contributions. (Mewaldt et al. 2005)

Tissue-Equivalent Proportional Counter

Rossi and Rosenzweig (1955) developed the concept of a tissue equivalent proportional counter (TEPC). The TEPC has convenient features that make it suitable and attractive for use in radiation monitoring, and these detectors are now used on the International Space Station (Badhwar 2002). The TEPC was originally designed to measure the energy imparted in microscopic-sized volumes of tissue. The simulation principle of the TEPC is based on the criterion that a spectrum of energy imparted in a small volume can be measured by replacing it with a much larger cavity containing tissue equivalent gas at low pressure. The TEPC measures individual energy deposition, instead of LET directly. Energy deposition, ε, is converted into lineal energy, y, which

has the same dimensions as LET. Thus, the TEPC is a very useful microdosimeter in mixed or unknown radiation field.

The physical quantity that is actually measured by a TEPC is the charge, which is proportional to the number of ion pairs created in the sensitive volume. Therefore, the sensitivity is limited to the lowest detectable charge, which is a single ion pair. The smallest diameter of a TEPC is also limited by the gas amplification technique used. At very low pressure, it is impossible to obtain a signal without the electron avalanche filling a significant fraction of the detector cavity. With the development of TEPC technology over the years, volumes as small as a few nm in equivalent diameter have been simulated successfully (Kliauga 1990).

The conventional TEPC used today has a solid wall made of tissue equivalent plastic surrounding a gas-filled cavity. However, proportional counters with solid walls show distortions in their pulse-height distributions due to the so-called wall effects (Kellerer 1971; Rossi et al. 1955; Zaider et al. 1996). The wall effect will cause more energy to be deposited in the site by δ-rays than would occur in a uniform medium. On the other hand, wall-less (actually grid-walled) proportional counters can be used to measure the distribution of lineal energy for a radiation field in laboratory settings (Kliauga et al. 1995). However, these detectors have not been used in routine dosimetry measurement because they are more difficult to build. Fortunately, new designs for grid-walled, cylindrical proportional counters have been developed recently, which provides both good electric field geometry and stable mechanical structure. These advances in

detector design make it possible to build a detector system consisting of a set of grid-walled, proportional counters, simulating tissue volumes of different diameters.

Size Effect

It is well known that the energy imparted per unit site diameter is a function of the site size as well as the charge and velocity of the charged particles depositing the energy. HZE particles can produce numerous energetic δ-rays, which will carry a significant fraction of the energy lost by the primary ion, away from its track. The lineal energy measured for the same particle in a different size site will differ because the diameter of the site determines the fraction of the δ-rays energy that will be included with that deposited by the primary particle. The lineal energy of a given radiation in a small volume will be lower than in a larger volume due to more energy being carried out of the site by δ-rays. On the other hand, the mean energy and range of these δ-rays depends on the velocity of the primary ion and the number of δ-rays depends on its charge. Particles with different velocity and charge may have the same LET, but will have different δ-ray ranges, so the frequency mean lineal energy measured in a given size site will be different (Guetersloh et al. 2004). As a result of these effects, the differences in the measurement may provide information to characterize the incident primary particles. We can study the mean lineal energy y_F as a function of particle energy (velocity) and charge. Comparison of the results of a series of such calculations for different site sizes can be used to characterize particles. This is the cornerstone of theory in this study of a multi-size detector system.

Solid-Walled Detector System

Recently it has become possible to simulate the response of a TEPC to HZE particles computationally. Powerful computer codes have been developed for large scale, accurate and comprehensive simulations of particle detectors used in complex physics experiments. Monte-Carlo simulations of a multiple-size, solid-walled detector system have been attempted and proved the ability of the detector system to characterize radiations (Wang 2006). The simulated site size was chosen as 2.5, 0.5 and 0.1 μm in the study for solid-walled detectors. The results show that such a group of site-size functions very well to manifest the size effect, which is determined by the geometry of solid-walled detectors, for various particles in a wide energy range. Various responses of the solid-walled detector system for particles with same velocity make it possible to characterize the velocity of incident particles. However, the simulation of 100 MeV/n proton events shows a broad lineal energy distribution in sites larger than 0.1 μm in diameter, which is partially caused by the electron scattering or wall effect. As a result, it is very hard to separate the protons events, which make up ~90% of the fluence in GCR, from the δ-ray events produced by other HZE particles. The unique spectral characteristics of proton tracks restrict the practicability of a solid-walled detector system in the space radiation environment (See Chapter IV).

Geant4 Toolkit

Monte Carlo simulations have become an indispensable tool for radiation transport calculations in a great variety of applications. The computer code Geant4

(Agostinelli et al. 2003; Allison et al. 2006) is attracting more interest because of its great versatility as a software toolkit for the simulation of the passage of particles through matter. Geant4 was the first, large-scale software project to pioneer the adoption of object-oriented technology in particles physics.

The Geant4 code contains a comprehensive range of physics models for electromagnetic, hadronic and optical interactions of a large set of particles over a wide energy range. It furthermore offers a diversity of tools for defining or importing the problem geometry for modeling complex, radiation sources and detection systems, including e.g., electromagnetic fields, electronic detector responses, time-dependences, and for exporting the required output data. Users of the Geant4 toolkit are responsible to select their own physics processes/models based on the physics object simulated, particle and energy range involved, simulation accuracy required, as well as experimental data library available.

The Geant4 modular architecture makes it possible for new components to be easily developed and integrated. The existing code is continuously being improved and extended with new functionalities according to new experimental results. For example, a number of developments and improvements have been made in the electromagnetic processes in recent Geant4 releases, which is of great importance in this research because δ-rays of low energy contribute a significant fraction of dose distribution. The standard electromagnetic package encompasses a new model-based design, concentrating the treatment of physics modeling in smaller, dedicated classes. The low-

energy, electromagnetic package addresses especially the requirement of precise simulation, extending Geant4 capabilities down to 250 eV.

CHAPTER III

PROCEDURES

Monte Carlo simulations were performed using the Geant4 toolkit (version 8.0.p01). The simulations were designed to match the conditions of solid-walled detectors by Wang (2006). It compiled the physics lists from the N03, underground physics (Howard and Araujo, 2003), and radioprotection (Cougnet et al. 2004) examples included in the Geant4 toolkit. The latter was used for hadronic interaction. Low energy physics models were implemented for all particles. The same physics list was used for all simulations. To increase the efficiency of the simulation using the Geant4 code, we specified a threshold in terms of range, a "cut value", for electron transport so that when an electron slowed down to an energy that corresponded to a range that was below the specified "cut value", the remaining energy is taken as depositing locally. According to Taddei et al. (2008), we finally chose the cut value of 10 μm. It was necessary to track electrons down to range of 10 μm or less because energy deposition is influenced by large numbers of low energy electrons with large transverse momentum. However, this low cut value did increase the computational time required to complete each simulation.

Particle Selection

In this work, fully stripped ions of ^{12}C, ^{16}O, ^{28}Si, ^{56}Fe ions were used as the primary particle, with ^{4}He and protons for comparison. This is because Carbon, oxygen, silicon and iron are among the nuclides with highest abundance in cosmic ray spectrum

(Fig. 2.4). On the other hand, nuclides with even-even proton-neutron number normally have the greatest abundance because of their superior stability (Kaplan 1956).

As shown in Fig. 2.3, the HZE particles have a large energy distribution range. The fluence rate is greatest in the ranges of 100 to 1000 MeV/nucleon. Each ion will be calculated with energy of 100, and 1000 MeV/nucleon, respectively. Simulations were performed separately for each particle type and energy combination.

Detector

For better comparison of solid-walled detector system (Wang 2006), the simulated site sizes of tissue volume are also chosen as 2.5, 0.5 and 0.1 μm. Propane at pressure of 33 Torr (4.40 kPa) was used as the tissue equivalent gas in the cavity as well as the vacuum chamber. Its density at standard temperature and pressure is 8.35×10^{-5} g/cm^3. The sites will be simulated by detector diameters of 31.75, 6.35 and 1.27 mm (1.25, 0.25 and 0.05 inch), respectively. The methodology used by Geant4 toolkit did not include variations in the transposition from energy deposition into measureable electronic signals. However, averaged quantities were faithfully reproduced.

Simulation Procedures

To calculate the energy deposition in a detector for a uniform radiation field of HZE particles, the most straightforward method is to generate a broad beam of charged particles with a diameter large enough that most of the δ-rays generated by an incremental increase in the diameter of the beam will not reach the detector located in

the center of the beam. It also means the radius of the "broad beams" should be comparable to the largest range of δ-rays generated by primary ions. A 600 MeV/nucleon $^{56}Fe^{26+}$ particle going through tissue will generate δ-rays, with the maximum energy of 1.75MeV, which are energetic enough to travel up to 8000 μm away from the path of the iron ion (Metting et al. 1988). This suggests that the diameter of a "board beam" may have to be thousands times that of the detector. As a result of the significant difference between the size of board beam and the detector, the probability that a δ-ray created by the beam will produce an event observed in the detector is extremely small. We may not be able to obtain results with satisfactory statistics after years of calculation because such low efficiency of simulation will boost the requirement of CPU time dramatically.

As an alternative method of simulation, we may divide the cross section of the board beam into numerous partitions and calculate the result of lineal energy distribution f(y) corresponding to the primary particles in each partition. One way to create these partitions is to divide the whole cross section into a series of concentric rings. The result of f(y) for the whole board beam will be achieved by summing the appropriately weighted results of f(y) for different partitions of the radiation field, in this case all the concentric rings.

As shown in Fig. 3-1, the simulation of f(y) for the first ring, as well as a circle area in the center of beam, will be conducted for a wall-less spherical detector with the diameter of d, sitting in the middle of a uniform cylindrical radiation field with the radius of b_0. Since the size of the radiation field is relatively small relative to the average

range of δ-rays, a large fraction of the primary particles in the beam will deposit some energy in the detector. To choose a proper value of b_0 for this approach, preliminary simulation will be made starting from $b_0=5d$ with an increment of d. The ratio of the total number of detected δ-ray events to that of all the simulated primary particles in this field is used to indicate the efficiency of calculation. b_0 used for the final simulation of $f_0(y)$ is obtained when the ratio is less than 1/10.

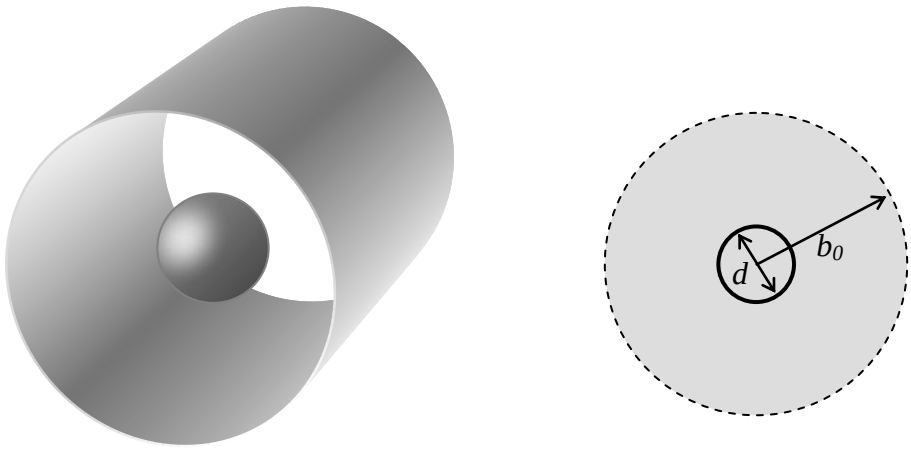

Figure 3.1. The model used for calculation of f(y) for the first partition of the "board beam". The space inside the cylinder in the left figure and the grey area in the right one represent the simulated radiation field.

For the second partition of the board beam, right outside of the first one, as shown in Fig. 3-2, we choose the diameter of detector d as the thickness of ring. The grey region in the right half of the figure represents the simulated radiation field. According to Geant4 calculations for energy deposition in a site as a function of the perpendicular distance (b) between a HZE ion track and the center of the site (Wang

2004), f(y) produced by δ-rays is essentially independent of b. On the other hand, the difference of b for the primary ions in the simulated field in this geometry is relatively smaller than the absolute value of b itself. Thus we may assume that all the primary ions in the field make approximately the same contribution to the total lineal energy distribution. In other words, we can obtain the result of $f_1(y)$ by simulating a detector with a distance of $b_0+d/2$ from the center of the detector and the primary ion track.

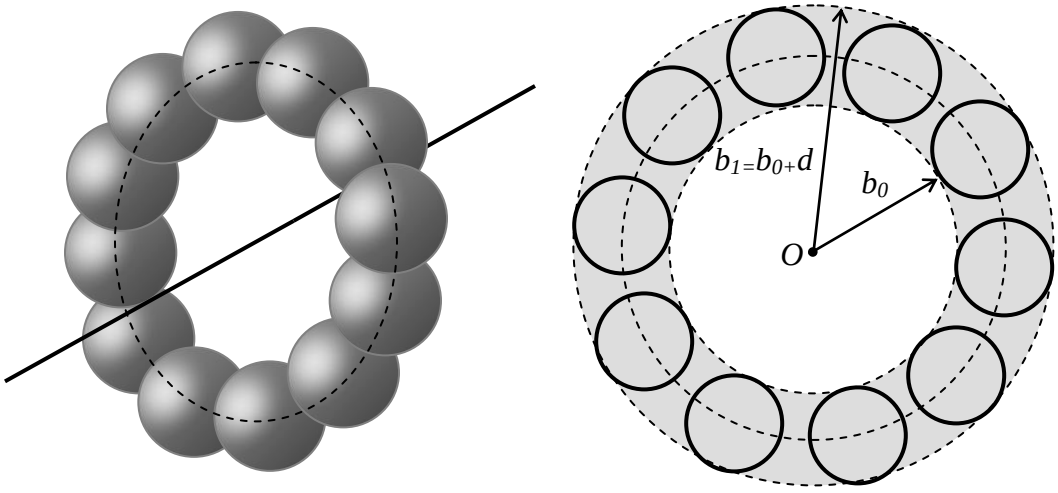

Figure 3.2. The detector and beam configuration for calculation of f(y) for the second partition of the "board beam". The grey area in the right figure represents the simulated radiation field. The solid line in the left figure shows the track of primary ions. The time required to calculate f(y) is reduced by replacing a single detector at O with 12 detectors in the ring.

To increase the efficiency of calculation, we can put a group of identical detectors in a ring with the same distance to the ion track, and use as many as possible without overlapping each other. Since the probability of producing one δ-ray event in the site by a primary track with $b<b_0$ is about 1/10, the average number of δ-ray events

produced by a primary track with $b_1=b_0+d/2$ in one detector would be lower but close to 1/10. Considering the total number of detectors is on the order of ten, we may assume that the primary tracks with $b_1=b_0+d/2$ have a chance of producing one δ-ray event in one of detectors.

This is an application of reciprocity. The energy deposition is the same if the detector is at the center and the primary ion tracks fill the shaded area, but the calculation is much more efficient if the detectors fill the shaded area. However, this approach is not good for the center of the beam because the shape of f(y) varies substantially when the value of b is small (Metting et al. 1988). Use of f(y) in detectors filling the shaded area in Fig. 3-1 to represent the f(y) in the detector at the center would introduce significant error to the final result. That is why we must calculate the lineal energy distribution for $b<5d$ by using a uniform beam $10d$ in diameter.

For the successive partitions of a board beam, we also use the method above by placing the detectors centered in a circle with the radius of b_2 and simulating the primary particles as a beam perpendicular to the plane of the circle at its center. By doing the rest in the same manner, we can get the lineal energy distribution for each partition, $f_2(y)$, $f_3(y)$, …, $f_n(y)$, and so on.

As we mentioned above, the total lineal energy distribution f(y) will be a sum of all the $f_n(y)$ times the corresponding weighting factors. For a specific distribution $f_n(y)$, the weighting factors w_n can be calculated as:

$$w_n = \frac{\Delta_n A_n}{P_n D_n} \tag{3.1}$$

where Δ_n is the total number of δ-ray events which deposit energy in any of the detectors, P_n is the total number of primary particles simulated, D_n is the sum of the cross sectional area of all the detectors and A_n is the cross sectional area of the simulated radiation field of the cylinder with average radius b_n.

Thus, after normalization, an approximation of the lineal energy distribution f(y) in the detector for the whole "board beam" becomes

$$f(y) = \frac{\sum_{i=0}^{n} w_n f_n(y)}{\int_0^{\infty} \sum_{i=0}^{n} w_n f_n(y)\, dy} = \frac{\sum_{i=0}^{n} w_n f_n(y)}{\sum_{i=0}^{n} w_n} \tag{3.2}$$

The calculation of $f_n(y)$ is terminated when the difference of mean lineal energy y_F derived from f(y) using the following equation

$$y_F = \int y f(y) dy \tag{3.3}$$

is less than 1% with a 10% increment in b.

However, adding δ-rays do not have much effect on y_F for helium ions and protons since the y for the primary is similar to y for the δ-rays. So the 1% criterion does not work for them. Since the maximum δ-ray range is the same for all the particles with same velocity, the maximum b used for helium ion and proton simulations was the same as the value of b at which the simulation of iron was terminated. Although calculation efficiency is pretty low when b is large for helium ions and protons, lower production of δ-ray events makes the CPU time for simulation of each incident proton and helium ion relatively shorter than that of iron and silicon ions. More primary particles can be simulated for protons and helium ions for better statistics of the results.

CHAPTER IV

RESULTS AND DISCUSSION

In this chapter, we discuss the results of the simulations. The calculations were performed for $^{56}Fe^{26+}$, $^{28}Si^{14+}$, $^{16}O^{8+}$, $^{12}C^{6+}$, $^{4}He^{2+}$ and protons. The energies used were 1000 and 100 MeV/nucleon for each particle. The diameters of the simulated sites were 2.5, 0.5 and 0.1μm. The detectors and chambers were filled with propane gas at a pressure of 33 Torr. The detailed geometry can be found in Chapter III.

Illustration

Iron particles make up a significant fraction of the GCR spectrum and contribute most to equivalent dose. Since LET is roughly proportional to the square of the particle charge, the iron particle generates more δ-rays than the lighter nuclei. The size effect is expected to be more distinct for iron particles. The 1000 MeV/nucleon $^{56}Fe^{26+}$ was chosen as an example of this study.

Fig. 4.1 shows several frequency distributions of δ-ray events produced by 1000 MeV/nucleon $^{56}Fe^{26+}$ particles in a 2.5 μm site for different partitions using the method discussed in Chapter III. The distribution with $0<b<5d$, where d is the site diameter, contains both primary events and δ-ray events. All other distributions present only δ-ray events. As we mentioned before, the lineal energy distribution no longer changes appreciably as a function of b when b is greater than $50d$. Based on these distributions

and the weighting factors derived from the relative δ-ray event frequencies, we are able to get the total lineal energy distribution using Eq. 3.3.

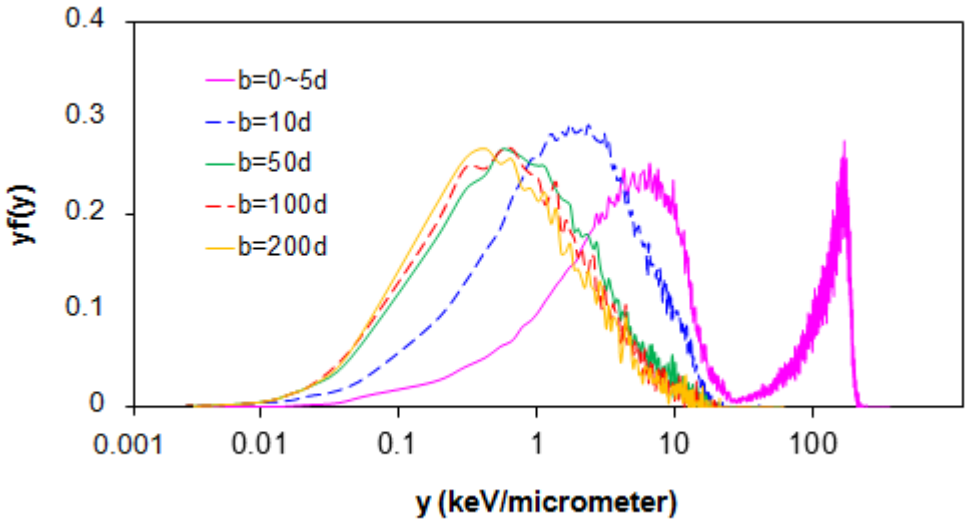

Figure 4.1. The frequency distribution, $yf(y)$, for 1000 MeV/nucleon $^{56}Fe^{26+}$ irradiating wall-less detectors simulating sites 2.5 μm in diameter as a function of b.

Fig. 4.2 shows the fraction of the δ-ray events for δ-ray equilibrium as a function of charged particle beam diameter. It demonstrates the frequency of δ-ray events at the center of a beam as a function of beam diameter expressed as a fraction of the frequency for a beam of infinite diameter. If the beam is not large enough (or the point of interest is too close to the edge of the beam), the number of δ-ray events per primary event will be reduced. Since equilibrium is not reached until the beam diameter is 1 cm for 1000 MeV/n particles, this can be significant in many biological experiments.

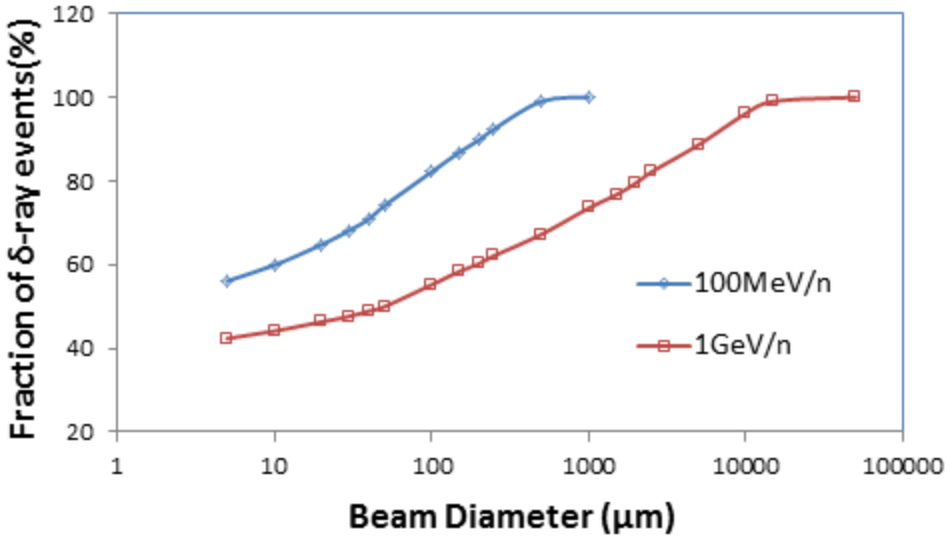

Figure 4.2. The fraction of δ-ray events for δ-ray equilibrium as a function of charged particle beam diameter for 1000 MeV/nucleon and 100 MeV/nucleon $^{56}Fe^{26+}$ irradiating wall-less detectors simulating sites 2.5 μm in diameter.

Fig. 4.3 shows the relative δ-ray event frequency *R* as a function of impact parameter. It is of radiobiological significance since this quantity indicates the probability of energy deposition in a site 2.5 μm in diameter when its center has an impact parameter, *b*, relative to a 1000 MeV/nucleon $^{56}Fe^{26+}$ ion trajectory.

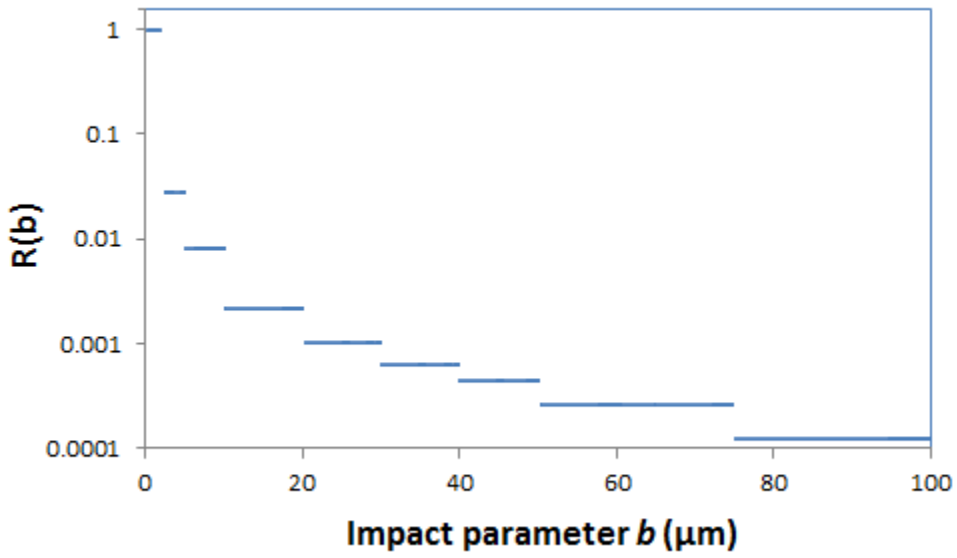

Figure 4.3. The relative δ-ray event frequency as a function of impact parameter *b* for 1000 MeV/nucleon $^{56}Fe^{26+}$ irradiating wall-less detectors simulating sites 2.5 µm in diameter.

Since there is no experimental data that exactly matches the simulation condition of this research to date, for the validation of simulation results, it is important to compare the Geant4 simulation with the homogeneous track models (Chatterjee and Schäefer 1976; Zhang, et al. 1985), which have be proved to show good agreement with experimental results (Metting 1988). Fig. 4.4 shows the comparison of radial dose calculations based on Geant4 simulations and homogeneous track structure model (Chatterjee and Schäefer 1976). It shows that the Geant4 simulation provides a good representation of radial doses deposited by 1000 MeV/nucleon $^{56}Fe^{26+}$ ions in sites 2.5 µm in diameter.

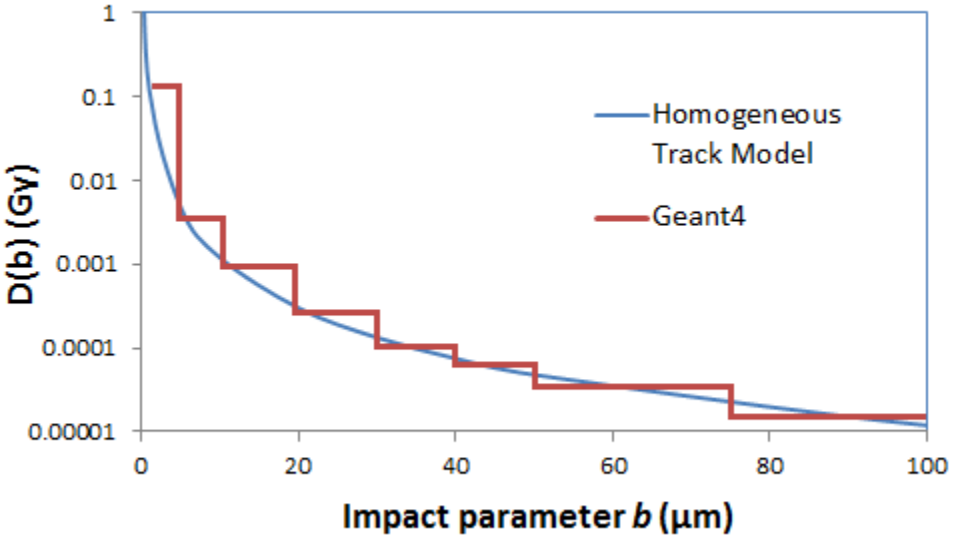

Figure 4.4. Comparison of radial dose calculations based on Geant4 simulations and homogeneous track structure model (Chatterjee and Schäefer 1976) for 1000 MeV/nucleon $^{56}Fe^{26+}$ ions irradiating wall-less detectors simulating sites 2.5 µm in diameter.

Fig. 4.5 shows the frequency distribution of events produced by 1000 MeV/nucleon $^{56}Fe^{26+}$ particles in different size sites. The distribution consists of two parts. The peak at the high lineal energy end is composed of energy deposition of both the primary particle and δ-rays when the primary particles cross the site. The position of the peak shifts to left slightly with decrease of the site size. This is because the δ-rays carry more energy out of the site due to the smaller site size. The low lineal energy portion of the curves is composed of events produced by δ-ray entering the site. The probability of δ-ray events increases as the site size decreases. This is because the average number of δ-ray events (in a site of a uniform medium with δ-ray equilibrium) per primary events is the amount of energy being carried outside the site by δ-rays of

primary particles that cross it divided by the average energy deposited per δ-ray event, which is approximately independent of the primary particles velocity, site diameter, or distance from the primary particle track to the site. There will also be more sites along each δ-ray track as the site size decreases. The increase in the probability of δ-ray events with decrease of the site size causes a decrease in the frequency mean lineal energy.

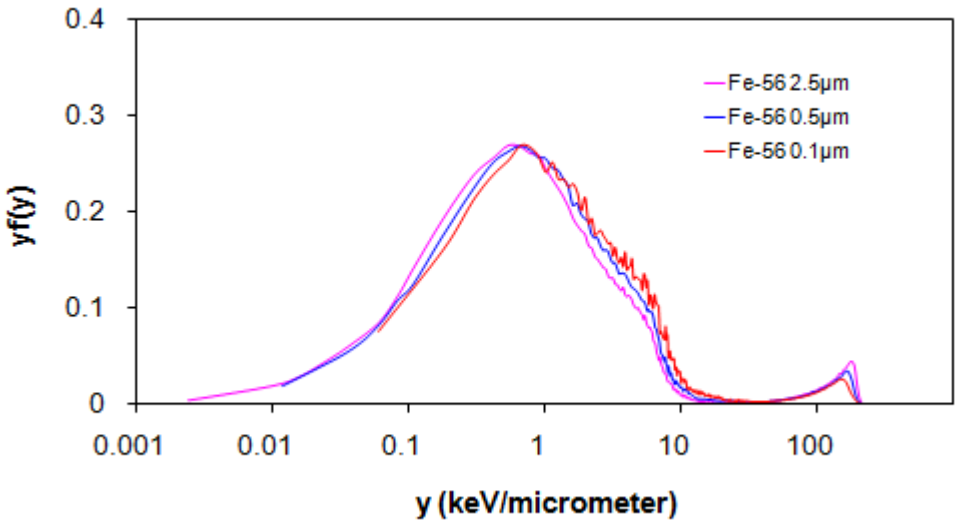

Figure 4.5. The frequency distribution, $yf(y)$, for a uniform broad beam of 1000 MeV/nucleon $^{56}Fe^{26+}$ irradiating wall-less detectors simulating sites ranging from 2.5, 0.5, and 0.1 µm in diameter.

The frequency mean, y_F is 4.60, 3.95 and 3.67 keV/µm for 2.5, 0.5 and 0.1 µm site sizes, respectively. Since the fractions of the events produced by the δ-rays and the primary particles are approximately proportional to areas under the left and right parts of the curve respectively, the ratio of these areas represents the average number of δ-ray events per primary event N_δ. The value is 34.7, 41.3 and 48.2 for 2.5, 0.5 and 0.1 µm site

sizes, respectively. These values are in agreement with Brooks et al. (2001) that 32 cells were hit by δ-rays for each cell that was traversed by the primary 1000 MeV/nucleon $^{56}Fe^{26+}$ particle. In fact, these values are calculated from the total number of primary tracks and the total number of δ-ray events which are obtained from the original data for different rings and the variable numbers of primary particles used for them. The reason we use this method instead of the one based on the ratio of two areas to calculate the value of N_δ is that it's very hard to distinguish the event produced by δ-ray events from the primary particles in the f(y) spectra for particles with small charges such as $^{4}He^{2+}$ particles and protons.

1000/100 MeV/nucleon $^{56}Fe^{26+}$ and $^{28}Si^{14+}$ Spectra

The simulation results of $^{56}Fe^{26+}$ and $^{28}Si^{14+}$ particles will be discussed in this section. Fig. 4.6 shows the frequency distribution of events produced by 100 MeV/nucleon $^{56}Fe^{26+}$ particles in different size sites. The frequency mean is 6.33, 4.82 and 3.91 keV/μm for 2.5, 0.5 and 0.1 μm site sizes, respectively. The number of δ-ray events per primary event is 83.2, 117 and 131 for 2.5, 0.5 and 0.1 μm site sizes, respectively. Fig. 4.7 shows the frequency distribution of events produced by 1000 MeV/nucleon $^{28}Si^{14+}$ particles in different size sites. The frequency mean is 4.40, 3.84 and 3.43 keV/μm for 2.5, 0.5 and 0.1 μm site sizes, respectively. The number of δ-ray events per primary event is 9.96, 12.0 and 13.9 for 2.5, 0.5 and 0.1 μm site sizes, respectively. Fig. 4.8 shows the frequency distribution of events produced by 100 MeV/nucleon $^{28}Si^{14+}$ particles in different size sites. The frequency mean is 6.16, 4.70

and 3.88 keV/μm for 2.5, 0.5 and 0.1 μm site sizes, respectively. The number of δ-ray events per primary event is 27.8, 34.7 and 42.4 for 2.5, 0.5 and 0.1 μm site sizes, respectively.

For each spectrum, we can see that the δ-ray distribution has relatively the same shape, independent of the primary particle velocity, charge and site diameter. For either particle, the peak produced by the primary events shifts to higher lineal energy when the particle energy decreasing from 1000 MeV/n to 100 MeV/n. This is because the primary particles with lower velocity have larger LET.

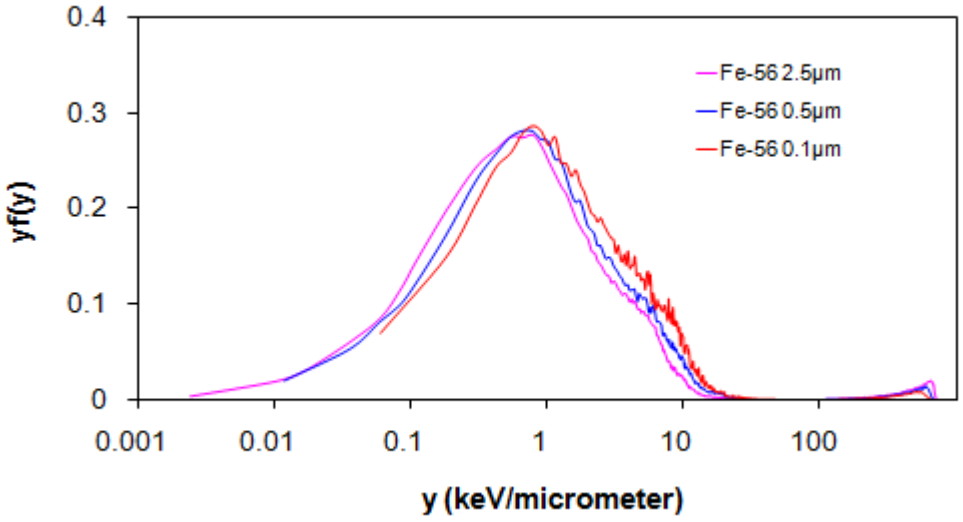

Figure 4.6. The frequency distribution, $yf(y)$, for a uniform broad beam of 100 MeV/nucleon $^{56}Fe^{26+}$ irradiating wall-less detectors simulating sites ranging from 2.5, 0.5, and 0.1 μm in diameter.

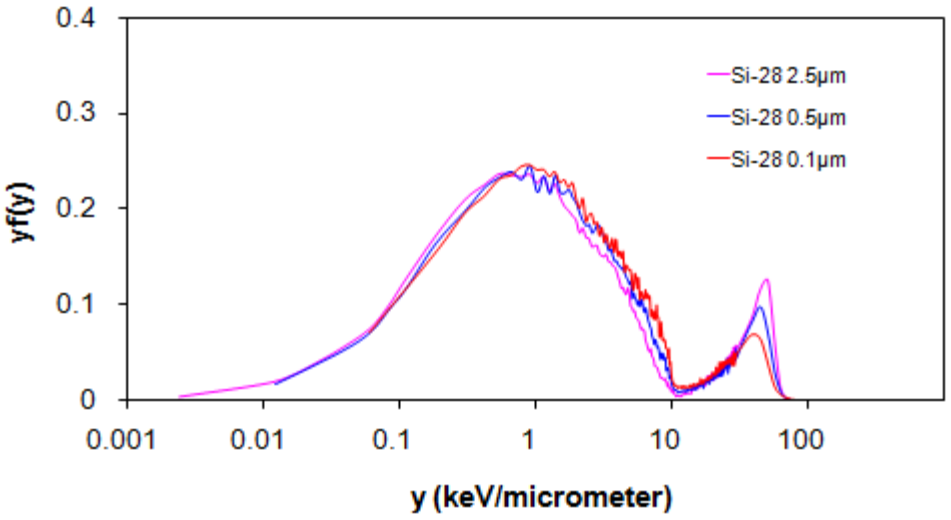

Figure 4.7. The frequency distribution, $yf(y)$, for a uniform broad beam of 1000 MeV/nucleon $^{28}Si^{14+}$ irradiating wall-less detectors simulating sites ranging from 2.5, 0.5, and 0.1 µm in diameter.

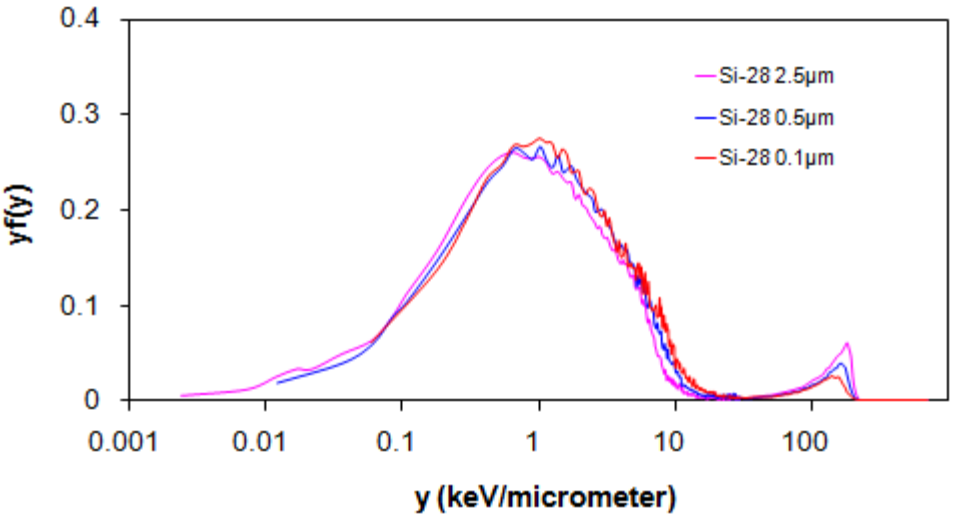

Figure 4.8 The frequency distribution, $yf(y)$, for a uniform broad beam of 100 MeV/nucleon $^{28}Si^{14+}$ irradiating wall-less detectors simulating sites ranging from 2.5, 0.5, and 0.1 µm in diameter.

Table 4.1 is the summary of y_F, the relative value of y_F, the number of δ-ray events per primary event N_δ, and the lineal energy y_P of the primary events between different site sizes irradiated by $^{56}Fe^{26+}$ particles. The y_F for a 2.5 μm site was taken as reference value (100%) for the relative y_F. For either energy, the frequency mean y_F is much smaller than the LET of primary particles. It is slightly larger for the particles with lower energy. Nevertheless, the lineal energy y_P of the primary events is comparable to the LET. And it becomes closer to the value of LET as the site size increases. This is because less δ-ray events produced by the primary ion deposit their energy outside the site. The number of δ-ray events per primary event is larger for 100 MeV/n $^{56}Fe^{26+}$ particles than 1000 MeV/n ones. That is because particles with lower velocity have larger LET and generate more δ-rays. The different fractions of δ-rays that escape causes the size effect. The more δ-rays being generated, the more variation occurs when the site size changes.

Table 4.2 is the summary of y_F, the relative value of y_F, the number of δ-ray events per primary event N_δ, and the lineal energy y_P of the primary events between different site sizes irradiated by $^{28}Si^{14+}$ particles. The difference between the results of two energies is similar to that of $^{56}Fe^{26+}$ particles. For $^{56}Fe^{26+}$ and $^{28}Si^{14+}$ particles with the same velocity, the number of δ-ray events per primary event is smaller for $^{28}Si^{14+}$ since the particles with less charge have smaller LET and generate less δ-rays.

Table 4.1. Lineal energy y_F, the relative value of y_F, the number of δ-ray events per primary event N_δ, and the lineal energy y_P of the primary events between different site sizes irradiated by $^{56}Fe^{26+}$ particles. The y_F of 2.5 μm site is taken as 100%.

Energy	LET	Site Size	2.5 μm	0.5 μm	0.1 μm
1000 MeV/n	149	y_F	4.60	3.95	3.57
		ratio	100%	85.9%	77.6%
		N_δ	34.7	41.3	48.2
		y_P	132	124	115
100 MeV/n	493	y_F	6.33	4.82	3.91
		ratio	100%	76.1%	61.8%
		N_δ	83.2	107	131
		y_P	450	412	345

Table 4.2. Lineal energy y_F, the relative value of y_F, the number of δ-ray events per primary event N_δ, and the lineal energy y_P of the primary events between different site sizes irradiated by $^{28}Si^{14+}$ particles. The y_F of 2.5 μm site is taken as 100%.

Energy	LET	Site Size	2.5 μm	0.5 μm	0.1 μm
1000 MeV/n	43.3	y_F	4.40	3.84	3.43
		ratio	100%	87.3%	78.0%
		N_δ	9.96	12.0	13.9
		y_P	38.6	36.0	32.7
100 MeV/n	143	y_F	6.16	4.70	3.88
		ratio	100%	76.3%	63.0%
		N_δ	27.8	34.7	42.4
		y_P	133	124	113

1000/100 MeV/nucleon $^{16}O^{8+}$ and $^{12}C^{6+}$ Spectra

With decrease of the particle charge, the $^{16}O^{8+}$ and $^{12}C^{6+}$ particles have smaller LET relative to $^{56}Fe^{26+}$ and $^{28}Si^{14+}$. This causes the peak produced by the primary particles to shift toward the low energy end and begin to merge with the curve produced by the δ-rays. The simulation results of $^{16}O^{8+}$ and $^{12}C^{6+}$ particles will be discussed in this section. Fig. 4.9 shows the frequency distribution of events produced by 1000 MeV/nucleon $^{16}O^{8+}$ particles in different size sites. The frequency mean is 4.04, 3.55 and 3.20 keV/μm for 2.5, 0.5 and 0.1 μm site sizes, respectively. The number of δ-ray events per primary event is 3.45, 4.05 and 4.73 for 2.5, 0.5 and 0.1 μm site sizes, respectively. Fig. 4.10 shows the frequency distribution of events produced by 100 MeV/nucleon $^{16}O^{8+}$ particles in different size sites. The frequency mean is 5.72, 4.51 and 3.77 keV/μm for 2.5, 0.5 and 0.1 μm site sizes, respectively. The number of δ-ray events per primary event is 8.14, 10.3 and 12.7 for 2.5, 0.5 and 0.1 μm site sizes, respectively.

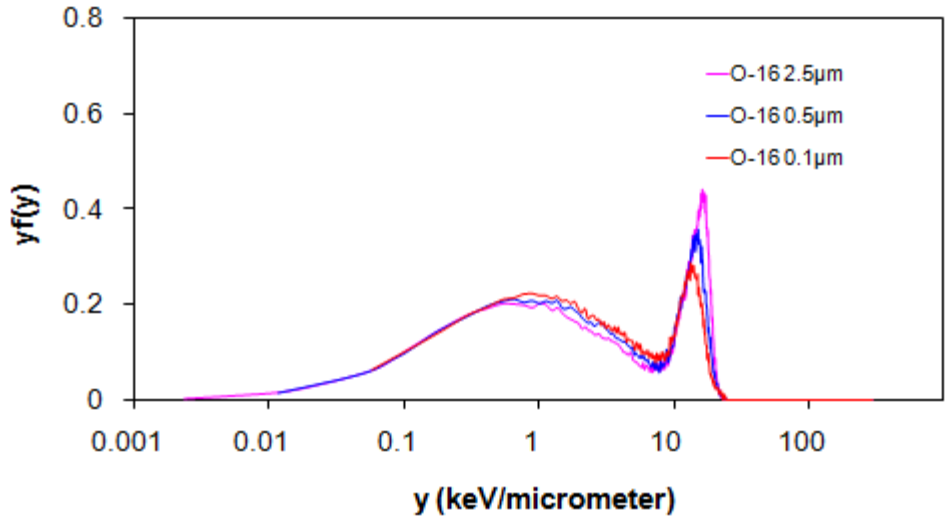

Figure 4.9. The frequency distribution, *yf*(*y*), for a uniform broad beam of 1000 MeV/nucleon $^{16}O^{8+}$ irradiating wall-less detectors simulating sites ranging from 2.5, 0.5, and 0.1 µm in diameter.

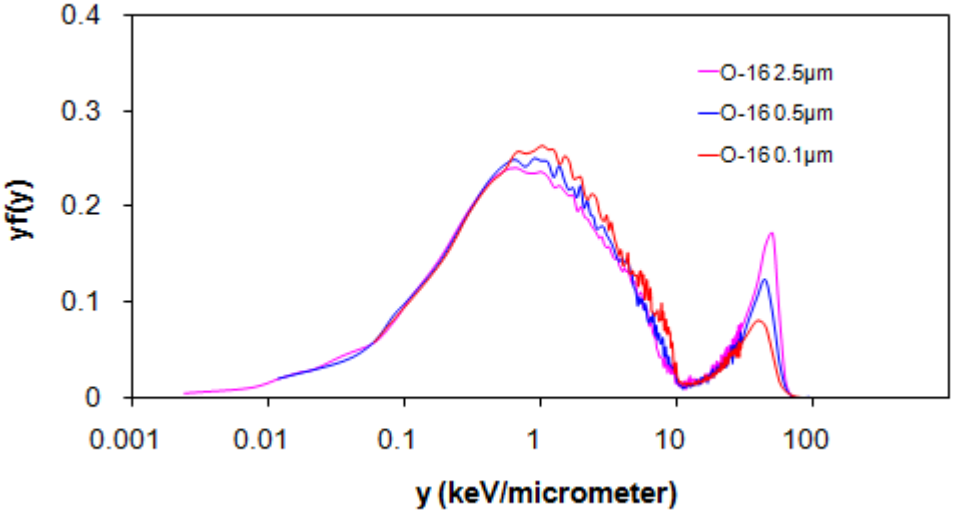

Figure 4.10. The frequency distribution, *yf*(*y*), for a uniform broad beam of 100 MeV/nucleon $^{16}O^{8+}$ irradiating wall-less detectors simulating sites ranging from 2.5, 0.5, and 0.1 µm in diameter.

It should be mentioned that there is some uncertainty in the number of δ-ray events per primary event for 1000 MeV/nucleon $^{16}O^{8+}$ particles if we calculate it from the ratio of two areas under the left and right parts of the curve. Using certain value, such as 10 KeV/ μm, as the cutoff edge for δ-ray distributions to calculate the fraction of events produced by δ-rays only may generate some error. Nevertheless, these numbers still shows that particles with smaller charge will produce less δ-ray events due to their smaller stopping power.

Fig. 4.11 shows the frequency distribution of events produced by 1000 MeV/nucleon $^{12}C^{6+}$ particles in different size sites. The frequency mean is 3.42, 3.07 and 2.78 keV/μm for 2.5, 0.5 and 0.1 μm site sizes, respectively. The number of δ-ray events per primary event is 1.74, 2.05 and 2.36 for 2.5, 0.5 and 0.1 μm site sizes, respectively. Fig. 4.12 shows the frequency distribution of events produced by 100 MeV/nucleon $^{12}C^{6+}$ particles in different size sites. The frequency mean is 5.00, 4.05 and 3.45 keV/μm for 2.5, 0.5 and 0.1 μm site sizes, respectively. The number of δ-ray events per primary event is 4.41, 5.56 and 6.82 for 2.5, 0.5 and 0.1 μm site sizes, respectively.

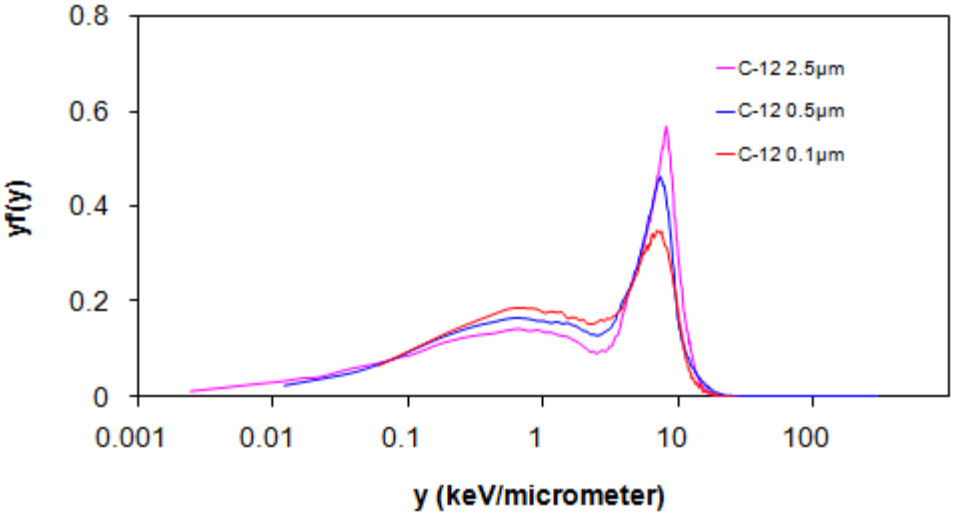

Figure 4.11. The frequency distribution, $yf(y)$, for a uniform broad beam of 1000 MeV/nucleon $^{12}C^{6+}$ irradiating wall-less detectors simulating sites ranging from 2.5, 0.5, and 0.1 µm in diameter.

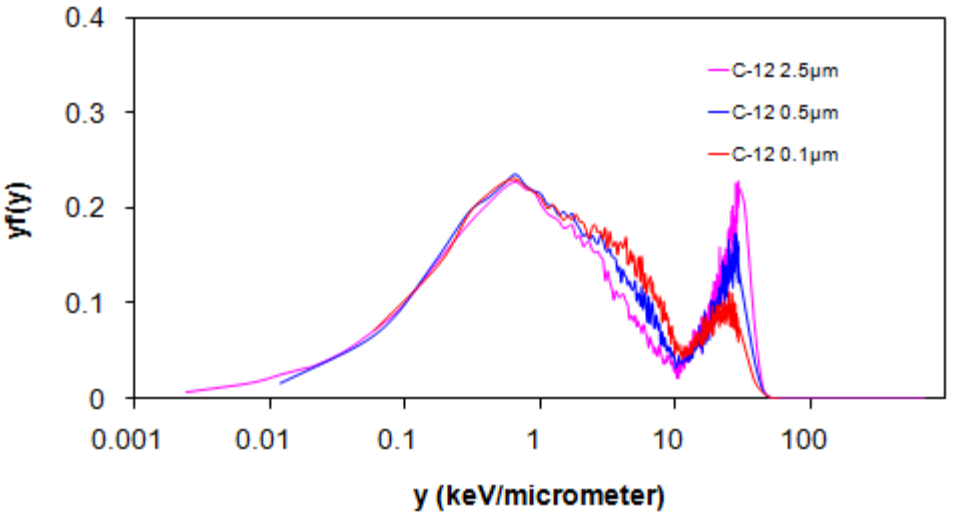

Figure 4.12. The frequency distribution, $yf(y)$, for a uniform broad beam of 100 MeV/nucleon $^{12}C^{6+}$ irradiating wall-less detectors simulating sites ranging from 2.5, 0.5, and 0.1 µm in diameter.

Table 4.3 and 4.4 are the summaries of y_F, the relative value of y_F and the number of δ-ray events per primary event N_δ between different site sizes irradiated by $^{16}O^{8+}$ and $^{12}C^{6+}$ particles respectively. The y_F of 2.5 μm site was taken as 100%.

Table 4.3. Lineal energy y_F, the relative value of y_F and the number of δ-ray events per primary event N_δ between different site sizes irradiated by $^{16}O^{8+}$ particles. The y_F of 2.5 μm site is taken as 100%.

Energy	LET	Site Size	2.5 μm	0.5 μm	0.1 μm
1000 MeV/n	14.1	y_F	4.04	3.55	3.20
		ratio	100%	87.9%	79.2%
		N_δ	3.45	4.05	4.73
100 MeV/n	46.7	y_F	5.72	4.51	3.77
		ratio	100%	78.8%	65.9%
		N_δ	8.14	10.3	12.7

Table 4.4. Lineal energy y_F, the relative value of y_F and the number of δ-ray events per primary event N_δ between different site sizes irradiated by $^{12}C^{6+}$ particles. The y_F of 2.5 μm site is taken as 100%.

Energy	LET	Site Size	2.5 μm	0.5 μm	0.1 μm
1000 MeV/n	7.96	y_F	3.42	3.07	2.78
		ratio	100%	89.8%	81.3%
		N_δ	1.74	2.05	2.36
100 MeV/n	26.2	y_F	5.00	4.05	3.45
		ratio	100%	81.0%	69.0%
		N_δ	4.41	5.56	6.82

Helium and Proton Spectra

The simulation results of $^{4}He^{2+}$ particles and protons will be discussed in this section. Fig. 4.13 shows the frequency distribution of events produced by 1000 MeV/nucleon $^{4}He^{2+}$ particles in different size sites. The frequency mean is 0.833, 0.806 and 0.778 keV/μm for 2.5, 0.5 and 0.1 μm site sizes, respectively. The number of δ-ray events per primary event is 0.528, 0.661 and 0.792 for 2.5, 0.5 and 0.1 μm site sizes, respectively. Fig. 4.14 shows the frequency distribution of events produced by 100 MeV/nucleon $^{4}He^{2+}$ particles in different size sites. The frequency mean are 2.04, 1.84 and 1.67 keV/μm for 2.5, 0.5 and 0.1 μm site sizes, respectively. The number of δ-ray events per primary event is 1.98, 2.33 and 2.67 for 2.5, 0.5 and 0.1 μm site sizes, respectively.

For 100 MeV/n $^{4}He^{2+}$ particles we can still see the left side distribution mostly produced by δ-ray events. However, we can hardly see any δ-ray distribution since the peak produced by the primary particles covers the same lineal energy range as δ-rays. That means the events produced by primary particles have about the same energy deposition as those produced by δ-rays.

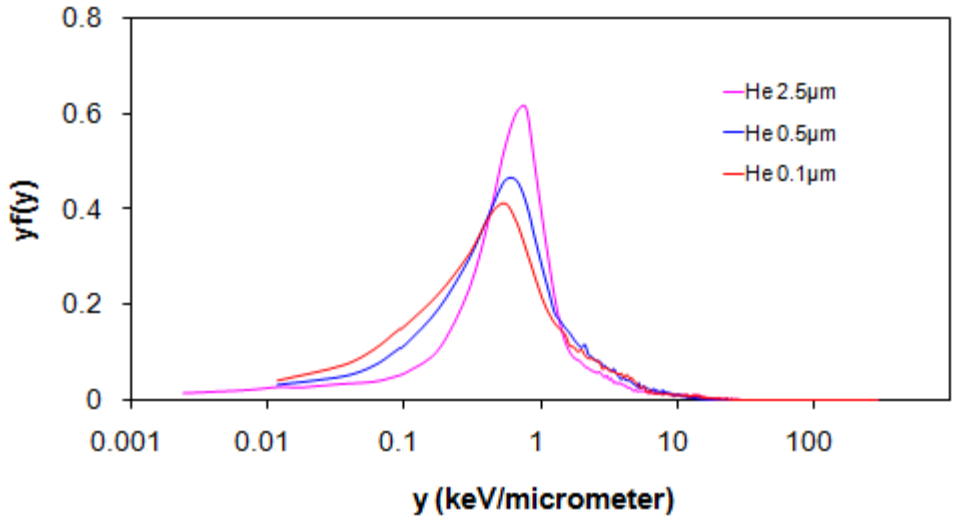

Figure 4.13. The frequency distribution, $yf(y)$, for a uniform broad beam of 1000 MeV/nucleon $^{4}He^{2+}$ irradiating wall-less detectors simulating sites ranging from 2.5, 0.5, and 0.1 µm in diameter.

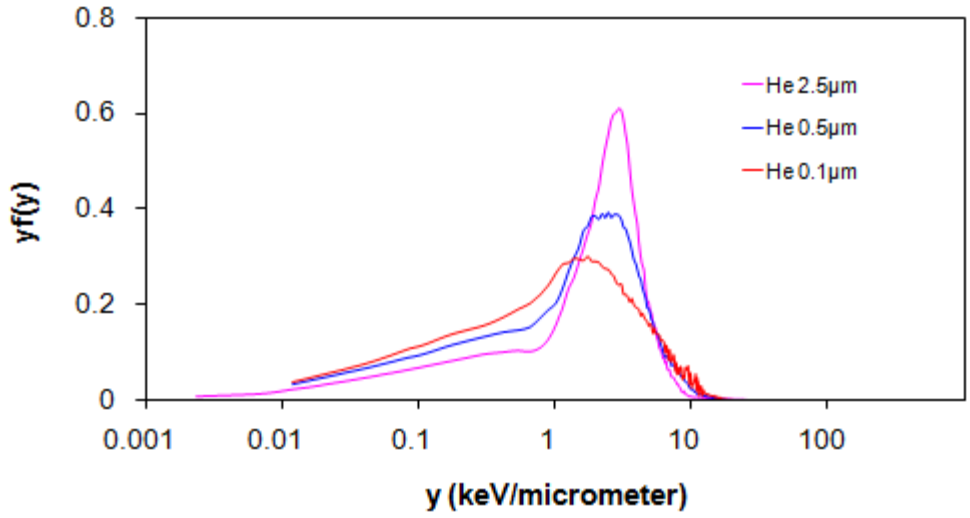

Figure 4.14. The frequency distribution, $yf(y)$, for a uniform broad beam of 100 MeV/nucleon $^{4}He^{2+}$ irradiating wall-less detectors simulating sites ranging from 2.5, 0.5, and 0.1 µm in diameter.

Fig. 4.15 shows the frequency distribution of events produced by 1000 MeV/nucleon protons in different size sites. The frequency mean is 0.219, 0.217 and 0.215 keV/μm for 2.5, 0.5 and 0.1 μm site sizes, respectively. The number of δ-ray events per primary event is 0.051, 0.059 and 0.068 for 2.5, 0.5 and 0.1 μm site sizes, respectively. Fig. 4.16 shows the frequency distribution of events produced by 100 MeV/nucleon protons in different size sites. The frequency mean is 0.734, 0.706 and 0.675 keV/μm for 2.5, 0.5 and 0.1 μm site sizes, respectively. The number of δ-ray per primary events is 0.120, 0.151 and 0.179 for 2.5, 0.5 and 0.1 μm site sizes, respectively.

In Fig. 4.15 and 4.16, the 0.1 μm spectra show a large event distribution peak at about 0.2 keV/μm and a sharp falling edge. In this small site, protons can go through the site with small possibility of producing a δ-ray. So the proton peak can be observed. The sharp edge indicates the maximum energy deposition by the protons going through from the center of the site. These are still a few δ-ray events on the right side of the peak, but their number is very small relative to the primary event because of the low stopping power of protons. Since very few events are produced by δ-rays, the lineal energy distributions of protons are nearly independent of site size. The proton tracks are long so the only thing left is a broadening of the peak at smaller site sizes due to the straggling.

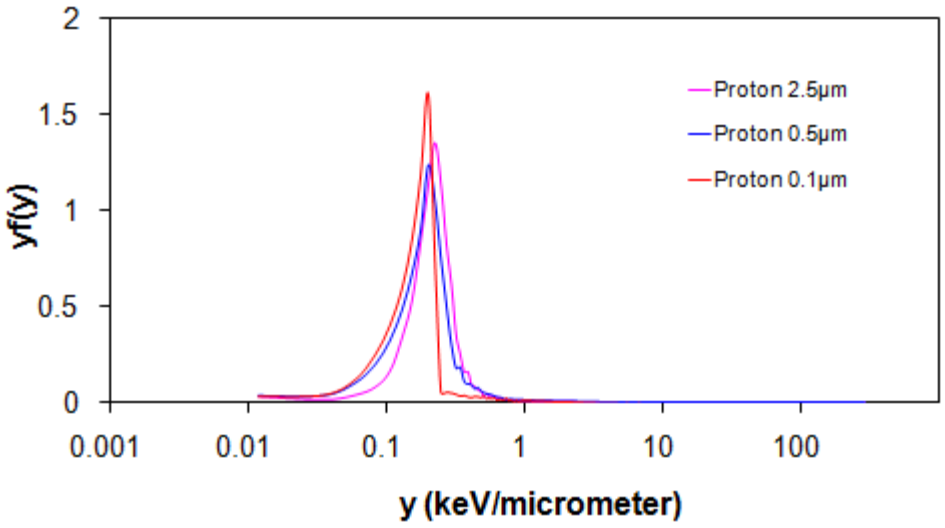

Figure 4.15. The frequency distribution, $yf(y)$, for a uniform broad beam of 1000 MeV/nucleon protons irradiating wall-less detectors simulating sites ranging from 2.5, 0.5, and 0.1 μm in diameter.

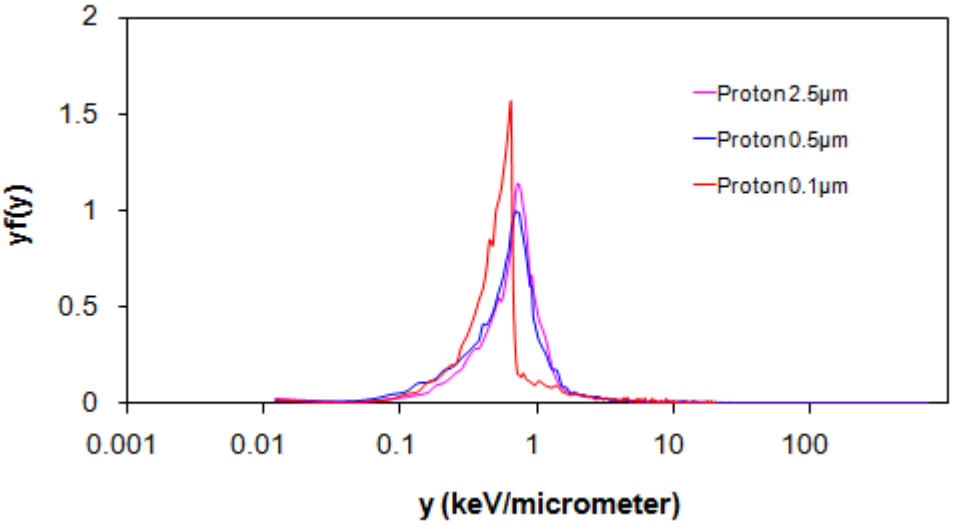

Figure 4.16. The frequency distribution, $yf(y)$, for a uniform broad beam of 100 MeV/nucleon protons irradiating wall-less detectors simulating sites ranging from 2.5, 0.5, and 0.1 μm in diameter.

Table 4.5 and 4.6 are the summaries of y_F, the relative value of y_F and the number of δ-ray events per primary event N_δ between different site sizes irradiated by $^4He^{2+}$ particles and protons respectively. The y_F of 2.5 μm site was taken as 100%. Unlike primary particles with larger charges, the y_F of $^4He^{2+}$ particles and protons is very close to their LETs. This is because the average energy deposited per unit path length (the mean lineal energy y_F) by high energy particles with low stopping power will not change significantly because the particle tracks are long and δ-ray that carry enough energy to significantly change y_F are rare. These results show that calculations by the Geant4 toolkit are in good agreement with the data published in ICRU report 49 (1993).

Table 4.5. Lineal energy y_F, the relative value of y_F and the number of δ-ray events per primary event N_δ between different site sizes irradiated by $^4He^{2+}$ particles. The y_F of 2.5 μm site is taken as 100%.

Energy	LET	Site Size	2.5 μm	0.5 μm	0.1 μm
1000 MeV/n	0.884	y_F	0.833	0.806	0.778
		ratio	100%	96.8%	93.4%
		N_δ	0.528	0.661	0.792
100 MeV/n	2.916	y_F	2.04	1.84	1.67
		ratio	100%	90.2%	81.9%
		N_δ	1.98	2.33	2.67

Table 4.6. Lineal energy y_F, the relative value of y_F and the number of δ-ray events per primary event N_δ between different site sizes irradiated by protons. The y_F of 2.5 μm site is taken as 100%.

Energy	LET	Site Size	2.5 μm	0.5 μm	0.1 μm
1000 MeV/n	0.221	y_F	0.219	0.217	0.215
		ratio	100%	99.1%	98.2%
		N_δ	0.051	0.059	0.068
100 MeV/n	0.729	y_F	0.734	0.706	0.675
		ratio	100%	96.2%	92.0%
		N_δ	0.120	0.151	0.179

Statistics Error

The y_F of all site sizes irradiating by each particle were obtained from single calculation. In this research, each total lineal energy distribution is calculated from multiple simulations of different partitions. No repeat calculation was performed due to shortage of CPU power. Therefore, it is impossible to derive the data error from the results directly. However, based on the Geant4 simulations of solid-walled detectors (Wang 2006), the stochastic error of the mean lineal energy y_F is within 1% from the simulation of 10,000 iron ions irradiating 2.5, 0.5 and 0.1 μm diameter size. Considering that the number of particles used for grid-walled detector simulations is more than 100,000 per calculation, it is reasonable to assume the y_F values of single calculations are close to the mean value of multiple calculations.

Lineal Energy and Particle Charge

With the results of lineal energy distribution from $^{56}Fe^{26+}$ to proton, we can investigate the relationship between the frequency mean lineal energy y_F and the particle charge (Z). Table 4.7 is the summary of y_F for different site sizes irradiated by primary particles with different charges. Fig. 4.17 and 4.18 shows the relationship between charge and lineal energy y_F for each site irradiated by 1000 MeV/n and 100 MeV/n. particles respectively.

Within the same size, the y_F is larger for particles with higher Z. $^{56}Fe^{26+}$ has the largest y_F among those simulated particles. It is because the increasing stopping power, including ionization and excitation ability of the primary particle. However, the decrease in y_F from high Z particle $^{56}Fe^{26+}$ to low Z particle $^{12}C^{6+}$ is not distinct. Although the LET of $^{56}Fe^{26+}$ particles is about 20 times larger than that of $^{12}C^{6}$, the decrease in y_F is just 25% in the 2.5 μm site irradiated by 1000 MeV/n particles. Higher stopping power of particles with higher Z will increase the total energy deposited by the primary particles, the corresponding increasing number of δ-rays with the lineal energy mostly under 10 KeV/ μm neutralize the effect. The combined influence of two factors results in the mean lineal energy y_F remaining relatively constant despite of decrease of the particle charge when Z is large than 8. For the $^{4}He^{2+}$ and proton, the mean lineal energy y_F is very close to LET of the primary particles because of the smaller number of δ-ray events due to low stopping power.

On the other hand, the same particle with lower energy has larger mean lineal energy y_F. The total effect of increasing LET of the primary particles and producing

more δ-rays still cause some increase of the y_F. However, the extent of increase is different between different site sizes.

Table 4.7. Lineal energy y_F between different site sizes irradiated by primary particles with different charge and energies.

Energy	Particle \ Site Size	2.5 μm	0.5 μm	0.1 μm
1000 MeV/n	$^{56}Fe^{26+}$	4.60	3.95	3.57
	$^{28}Si^{14+}$	4.40	3.84	3.43
	$^{16}O^{8+}$	4.04	3.55	3.20
	$^{12}C^{6+}$	3.42	3.07	2.78
	$^{4}He^{2+}$	0.833	0.806	0.778
	Proton	0.219	0.217	0.215
100 MeV/n	$^{56}Fe^{26+}$	6.33	4.82	3.91
	$^{28}Si^{14+}$	6.16	4.70	3.88
	$^{16}O^{8+}$	5.72	4.51	3.77
	$^{12}C^{6+}$	5.00	4.05	3.45
	$^{4}He^{2+}$	2.04	1.84	1.67
	Proton	0.734	0.706	0.675

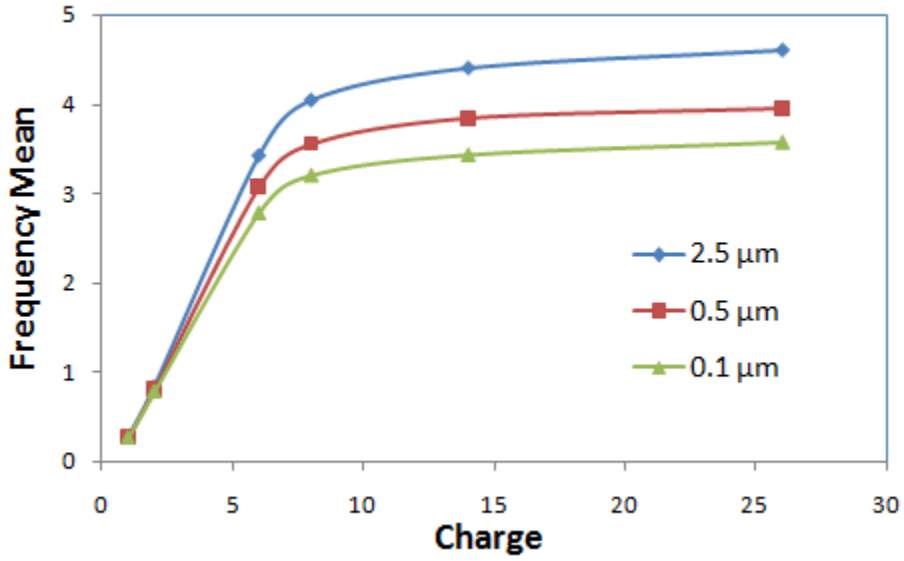

Figure 4.17. The relationship between charge and lineal energy y_F for each site irradiated by 1000 MeV/n particles.

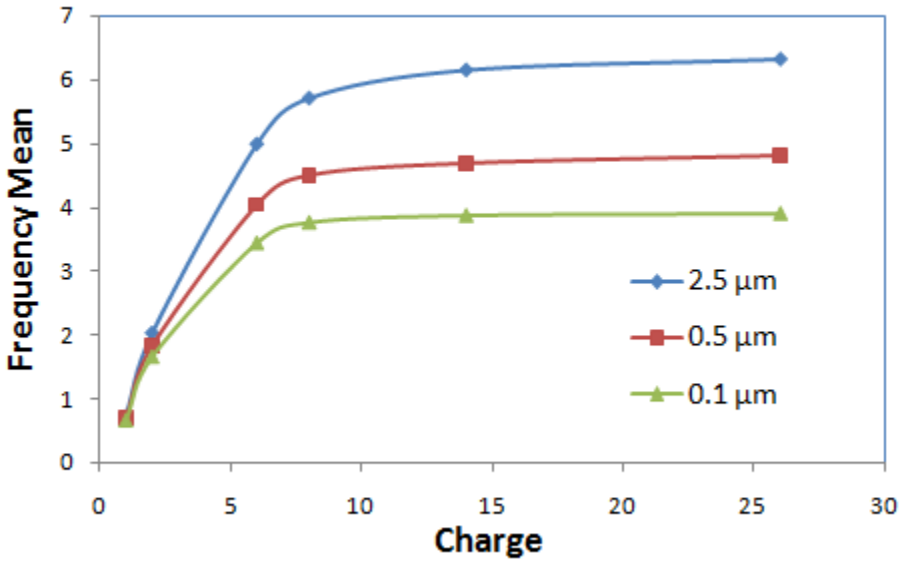

Figure 4.18. The relationship between charge and lineal energy y_F for each site irradiated by 100 MeV/n particles.

Consistency of Size Effect

It is worthwhile to check if the detector system shows consistent size effect to different energy particles. If there is constancy in the data, the detector system can be put into practical use for a much wider range of particles and energy with more confidence. Size effect is measured as the decrease of the lineal energy with decrease of the site size. Table 4.8 is the summary of the relative value of lineal energy y_F between different site sizes irradiated by primary particles with different charge and energies. The y_F of 2.5 µm site is taken as 100%. Fig. 4.19 shows the consistency of the size effect.

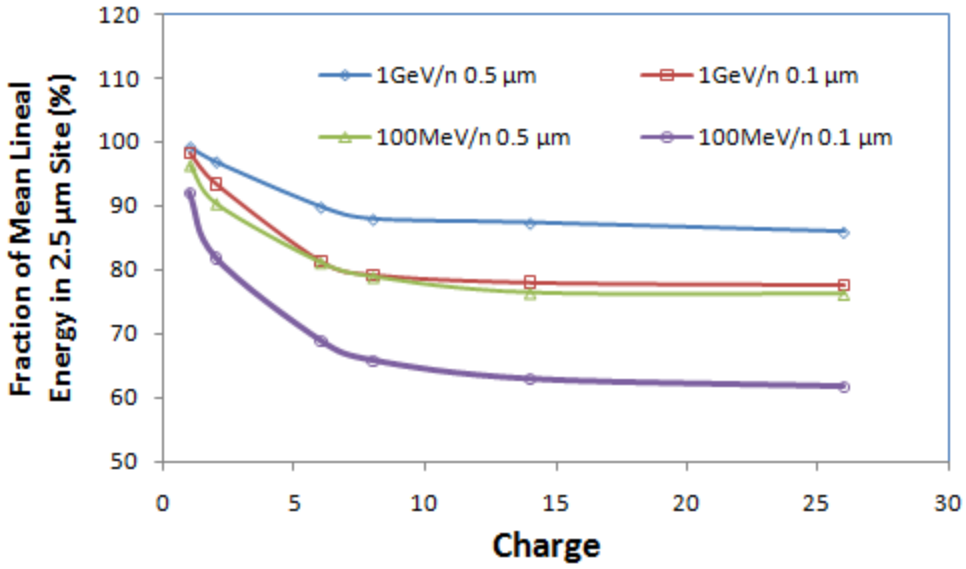

Figure 4.19. Size effect of particles of different Z in 0.5 and 0.1 µm site. The energy used was 1000 MeV/n and 100 MeV/n. The ordinate is the ratio of y_F with y_F of 2.5 µm site as the denominator. The abscissa is the charge of the primary particles. The particles involved are hydrogen, helium, carbon, oxygen, silicon and iron, from left to right.

Table 4.8. The relative value of lineal energy y_F between different site sizes irradiated by primary particles with different charge and energies. The y_F of 2.5 μm site is taken as 100%.

Energy	Site Size / Particle	2.5 μm	0.5 μm	0.1 μm
1000 MeV/n	$^{56}Fe^{26+}$	100%	85.9%	77.6%
	$^{28}Si^{14+}$	100%	87.3%	78.0%
	$^{16}O^{8+}$	100%	87.9%	79.2%
	$^{12}C^{6+}$	100%	89.8%	81.3%
	$^{4}He^{2+}$	100%	96.8%	93.4%
	Proton	100%	99.1%	98.2%
100 MeV/n	$^{56}Fe^{26+}$	100%	76.1%	61.8%
	$^{28}Si^{14+}$	100%	76.3%	63%
	$^{16}O^{8+}$	100%	78.8%	65.9%
	$^{12}C^{6+}$	100%	81%	69.0%
	$^{4}He^{2+}$	100%	90.2%	81.9%
	Proton	100%	96.2%	92%

For all particles with Z larger than 8, the size effect is consistent regardless the change of LET of the primary particles as well as the average number of δ-ray events per primary events. For $^{12}C^{6+}$ particles, size effect is still obvious but it becomes smaller relative to that of the particles with higher Z. For protons and $^{4}He^{2+}$ particles, size effect is not very notable since very few events are produced by δ-rays. For the HZE particles, the size effect becomes weakened as the energy increases. The y_F of 1000 MeV/nucleon particles changes less between the different size sites than that of 100 MeV/n particles.

This is true because the particles with the same Z but lower velocity produce more δ-ray events due to their larger stopping power and magnify the size effect.

Mixed Spectrum

Practically, the detector system will be used in an isotropic, mixed field. The system's ability to characterize particles in such a field should be studied by combining simulation results for various particles in a wider energy range than can be done here. We will only have a brief discussion based on the current results.

Firstly, we consider the simplest situation where there is a mixed field composed of monoenergetic protons and particles with same velocity. The collections of distribution curves for 1000 and 100 MeV/n particles in 0.1 μm diameter sites are shown in Fig. 4.20 and 4.21 respectively. When the measurement is done in a mixed field, the distribution of events produced by δ-rays for each particle will overlap with each other except for that produced by protons. As we have mentioned before, the frequency mean lineal energy y_F for particles with Z>6 does not change much as Z increases (Fig. 4.17 and 4.18). Since the lineal energy distribution for protons is quite different from that produced by δ-rays and is almost independent of site size, we can easily distinguish events produced by protons from other events in the spectrum. Since the mean lineal energy increases as the particle velocity decreases, the mean lineal energy for all the events other than protons will provide the information on the particle velocity or the energy. Furthermore, the particle energy can be verified by the size effect of the system. Because the size effect is relatively consistent for all the particles with Z>6 (Fig. 4.19),

the change of the mean lineal energy y_F for particles other than proton in detectors with different sizes is also an index of the particle energy. There are two methods to distinguish particles with different Z. Since particles with different Z have different stopping powers, the peak produced by the primary particles will have different maxima. However, peaks for particles with similar Z-values may overlap with each other and make it impossible to calculate the exact Z-value for each particle. The other method is to calculate the fraction of events produced by δ-rays or the average number of δ-rays per primary events for detectors with different sizes. The magnitude of change for different site size may give enough difference between particles with different Z and can be used as information characterizing the incident particles. Further calculation and analysis are needed to test this method.

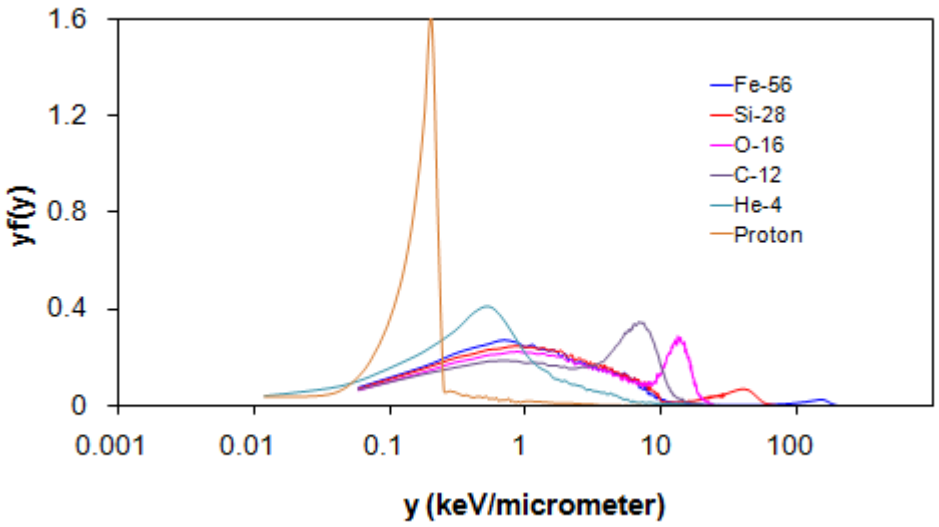

Figure 4.20. The frequency distribution, *yf*(*y*), of 1000 MeV/nucleon ions irradiating grid-walled detectors simulating sites 0.1 μm in diameter.

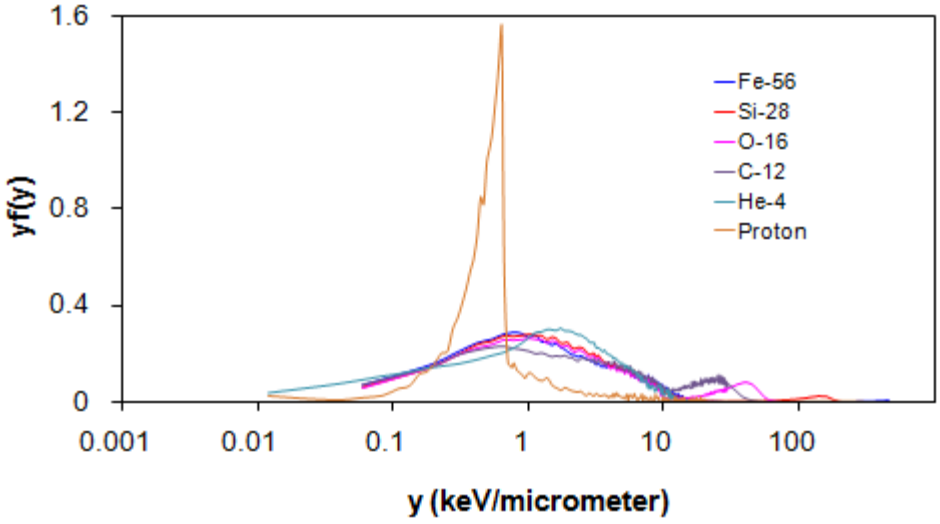

Figure 4.21. The frequency distribution, *yf*(*y*), of 100 MeV/nucleon ions irradiating grid-walled detectors simulating sites 0.1 μm in diameter.

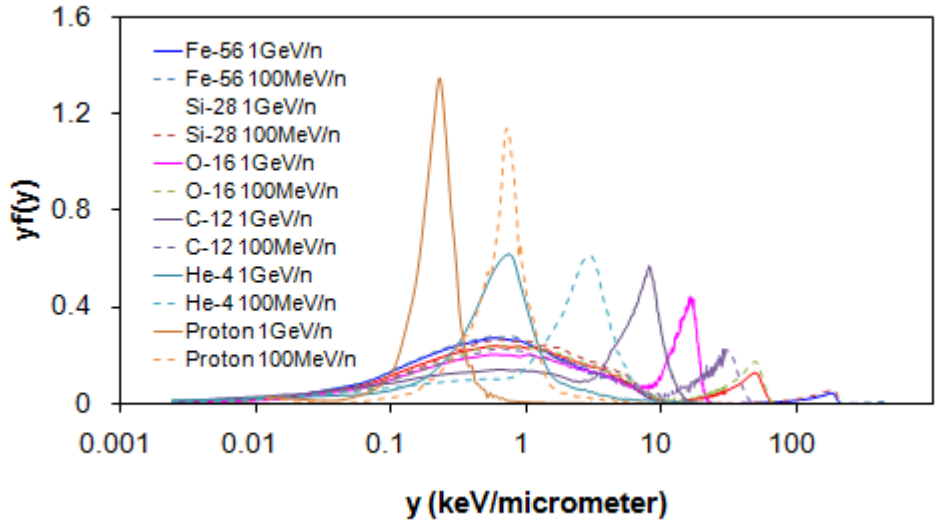

Figure 4.22. The frequency distribution, *yf*(*y*), of 1000 and 100 MeV/nucleon ions irradiating grid-walled detectors simulating sites 2.5 μm in diameter.

In reality, incident particles are not mono-energetic but within some energy range. To simplify the simulation, consider a radiation field consists of HZE particles with two different energies 1000 MeV/n and 100 MeV/n. The collection of distributions in a 2.5 μm diameter site was shown in Fig. 4.22. When the measurement is done in a mixed field, the peaks produced by primary particles will overlap each other. For example, the peak of 1000 MeV/nucleon $^{56}Fe^{26+}$ overlaps with 100 MeV/nucleon $^{28}Si^{14+}$, and the peak of 1000 MeV/nucleon $^{28}Si^{14+}$ overlap with 100 MeV/nucleon $^{16}O^{8+}$. Considering that we can distinguish the proton events from the distribution of events produced by δ-rays and primary particles other than protons as we have done before, we have no trouble calculating the mean lineal energy for all the HZE particles. Because the particles with the same velocity have almost the same mean lineal energy, the ratio of the total numbers of particles with two different energies can be calculated from the average mean lineal energy of the whole distribution. That means we can determine the fraction of the HZE particles in 2 energy bins if we only use one detector. Fig 4.23 shows the frequency distribution of events produced by a mixed ion beam consisting of 90% protons, 2% $^{4}He^{2+}$, 2% $^{12}C^{6+}$, 2% $^{16}O^{8+}$, 2% $^{28}Si^{14+}$, and 2% $^{56}Fe^{26+}$ in a 0.1 μm diameter site. The percentages of ions with two different energies 1000 MeV/n and 100 MeV/n are 70% and 30% respectively. After separating protons from the total spectrum, we can get the lineal energy distribution of events produced by other particles and calculate the mean lineal energy. Applying the method mentioned above and using the data obtained from this research, we can calculate the percentages of 1000 MeV/n and 100 MeV/n ions are 67% and 33% respectively (Appendix).

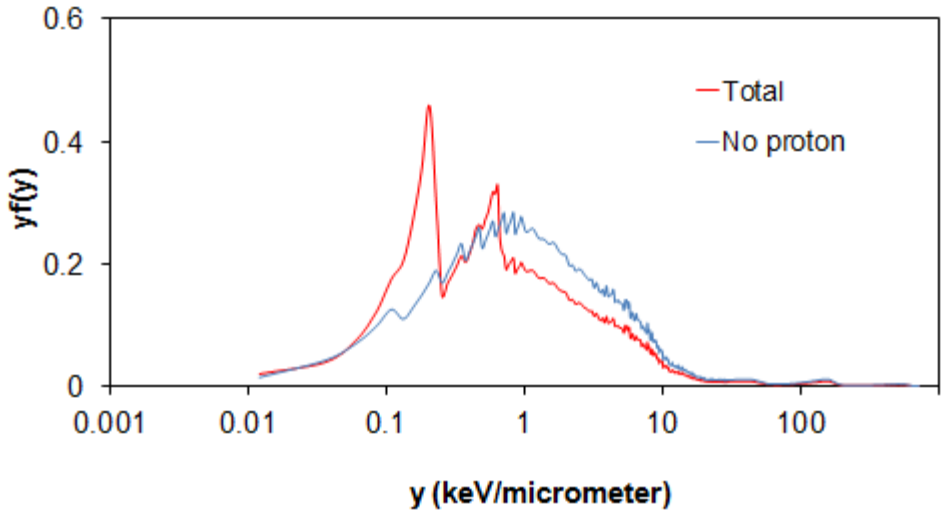

Figure 4.23. The frequency distribution, *yf*(*y*), of a mixed 70% 1000 MeV/nucleon and 30% 100 MeV/nucleon ion beam (consisting of 90% protons, 2% $^{4}He^{2+}$, 2% $^{12}C^{6+}$, 2% $^{16}O^{8+}$, 2% $^{28}Si^{14+}$, and 2% $^{56}Fe^{26+}$) irradiating grid-walled detectors simulating sites 0.1 μm in diameter.

For particles with a distribution within a continuous energy range, we can determine the fraction of the HZE particles in 4 different energy bins since we have detectors of 3 different sizes. The information of the particle charge can also be calculated with the method above but will be more complicated to accomplish. If two detector systems are used with and without shielding, the fragment generated in the shielding will modify the profile of the spectrum. This will also helpful to get information on the composition of the field. This would be future work which has not been included in this calculation.

It is inspiring to prove that this multi-size detector system is capable of characterizing particles with different velocity and charge. Obviously, the detectors can

also provide information that a normal proportional counter can do, such as dose, dose mean and mean lineal energy. It certainly can provide more routes to determine the dose and characterize the incident particle. A detector system with a similar design can be built to study further its practicability.

Comparison with Solid-Walled Detectors

Monte-Carlo simulations of a multiple-size, solid-walled detector system have been conducted by Wang (2006). It is worthwhile to compare the results of two (grid-walled and solid-walled) detector systems to demonstrate their advantages and disadvantage. We can see the impact of the wall effect of solid-walled detectors on the lineal energy distribution, the frequency mean energy y_F and the size effect. The comparison also shows the practicability of both systems if they are applied to characterize the HZE particles in galactic cosmic rays.

The site sizes simulated for solid-walled detectors are 2.5, 0.5 and 0.1 μm, same as those of grid-walled detectors. The cavities and chambers were also filled with propane gas at a pressure of 33 Torr. The difference is that solid-walled detectors have a 2-mm wall made of water with unit density. The depth of wall was chosen thick enough to stop the δ-rays generated outside of the wall by incident particles. Thus, a parallel beam with the diameter of the detector was used in the simulation. The energies of incident particles being used for simulation were 1000, 500 and 100 MeV/n.

Figs. 4.24 and 4.25 show the frequency distribution of 1000 and 100 MeV/nucleon $^{56}Fe^{26+}$ particles in different size sites for solid-walled detectors,

respectively. For better comparison, Fig 4.26 shows both distributions for solid-walled and wall-less detectors. The peaks on the right produced by the primary events are within the same energy range as those of the grid-walled detector distributions. Because the incident particles lose a very small fraction of their energy crossing the walls of the detectors and the cavities inside the detectors are also filled with propane gas at the same pressure, the distribution of the events produced by the primary particles should be similar for the grid and solid-walled detectors. Nevertheless, the mean lineal energy *y* for the primary ion peaks are higher for solid-walled detectors since some δ-rays are scattered back and deposit energy within the site. Furthermore, the peaks of the solid-walled detectors are more obvious than those of grid-walled detectors. This means the fractions of the primary events are larger, or the fractions of the δ-ray events are smaller, in solid-walled detectors than in grid-walled ones. As a result, the average number of δ-ray events per primary events is much smaller for the solid-walled detectors. The mean lineal energy y_F is also higher for solid-walled detectors.

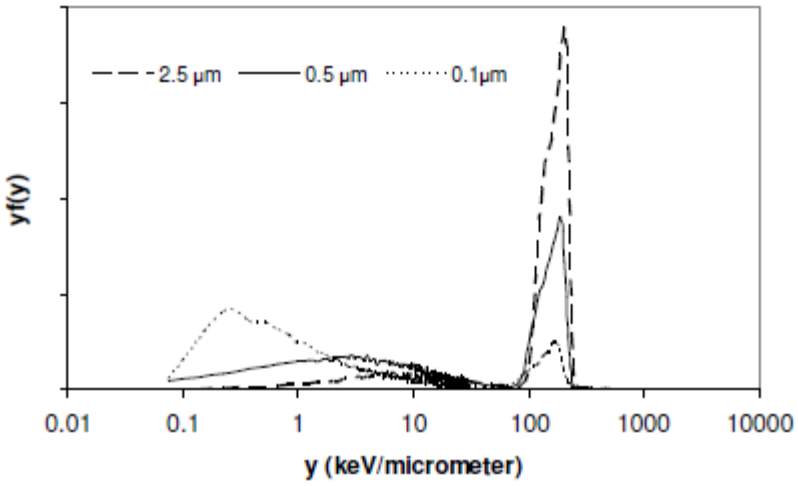

Figure 4.24. The frequency distribution, *yf*(*y*), for a uniform broad beam of 1000 MeV/nucleon iron ions irradiating solid-walled detectors simulating sites 2.5, 0.5, and 0.1 µm in diameter. (Wang 2006)

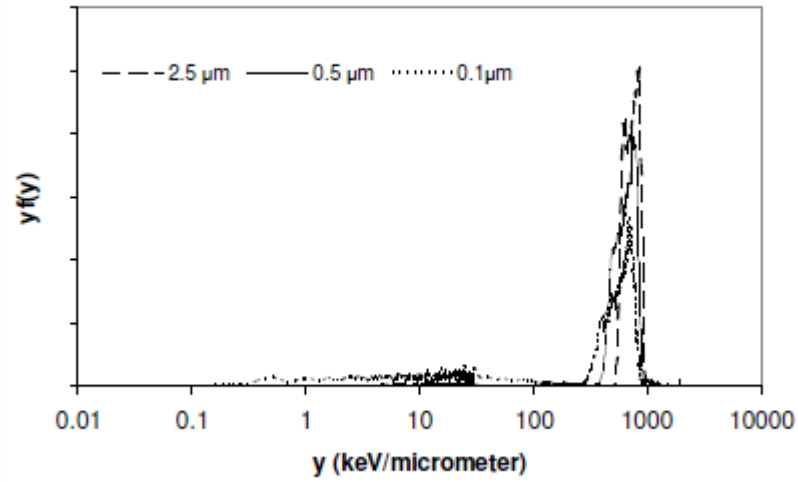

Figure 4.25. The frequency distribution, *yf*(*y*), for a uniform broad beam of 100 MeV/nucleon iron ions irradiating solid-walled detectors simulating sites 2.5, 0.5, and 0.1 µm in diameter. (Wang 2006)

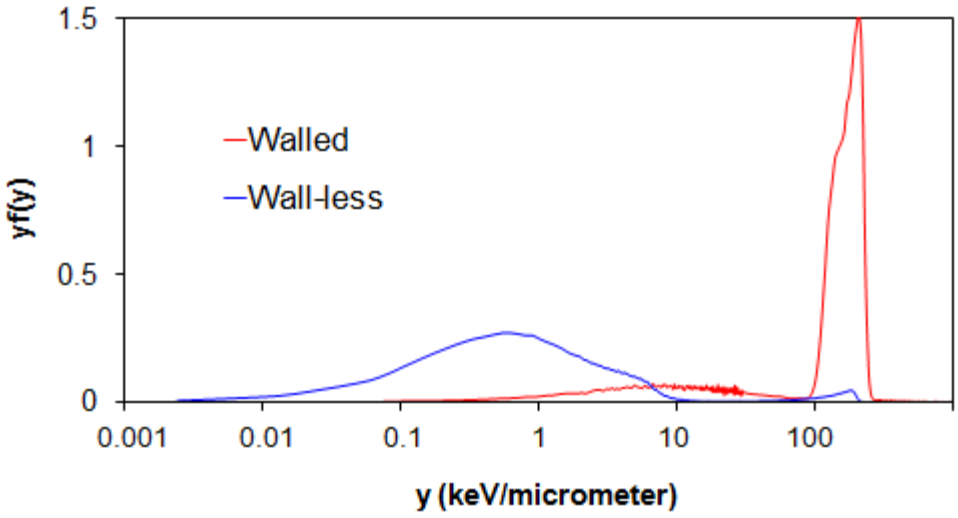

Figure 4.26. Comparison of the frequency distributions, *yf*(*y*), for a uniform broad beam of 1000 MeV/nucleon iron ions irradiating solid-walled/wall-less detectors simulating sites 2.5 μm in diameter.

We can explain it according to the geometry of solid-walled detectors and the process of simulation. As we have mentioned above, the thickness of the wall is 2 mm. For 0.1 μm site size, the cavity used in the simulation is 1.27 mm (0.05 inch) in diameter. Because the wall was thick enough to stop the δ-rays generated outside of the wall by incident particles, a parallel beam with the diameter of the detector was used in the simulation. Only the bombardment in the wall can generate δ-ray events in the site. The number of δ-ray events is proportional to the number of primary particles hitting the wall the detector. In other words, it is proportional to the cross-section area of the detector wall which is 2mm thick in this simulation since the beam was uniformly distributed within the diameter of the wall. However, a board beam with the diameter in the order of the maximum δ-ray range is used for grid-walled detector simulation. Since

the whole chamber is filled with 33 Torr propane gas, the beam diameter is about 10^5 times larger than that of the cavity. Thus the ratio of the fraction of incident particles outside and inside the cavity is dramatically larger for the grid-walled detector than for the solid-walled one. It is why we can see much more events produced by δ-rays in grid-walled detectors.

In contrast with grid-walled detectors, we can see from their lineal energy distributions that the average number of δ-rays events per primary events is less for 100 MeV/n particles than that of 1000 MeV/n ones, for solid-walled detectors. Although 100 MeV/n iron particles generate more δ-rays due to their higher stopping power than do the 1000 MeV/n particles, the δ-rays of a 1000 MeV/n iron are more energetic than those of 100 MeV/n particles. The δ-rays of 1000 MeV/n iron particles have larger possibility to penetrate the wall and enter the site while most of the δ-rays generated by 100 MeV/n particles are stopped within the wall.

On the other hand, the fraction of δ-rays with lineal energy greater than 10 KeV/μm is larger in the distributions of solid-walled detectors than those of grid-walled ones. The major reason is the δ-ray effect and the re-entry component of the wall effect. The δ-ray effect means two or more δ-rays enter the cavity together, but it will not happen in a uniform density medium because the distance between δ-rays is large enough that only one of them can enter the actual site. The re-entry effect means an electron may re-enter a cavity after it has traversed it due to its winding backwards path. The points of exit and re-entrance may be too far apart for the electron re-enter the site with uniform density. Both effects will cause the total energy deposited per δ-ray events

to be larger than that by a single electron entering the cavity once. However, the wall effect may not fully explain all the difference between the distributions of two detector systems. Further study is required to provide more information and a detailed explanation.

Table 4.9. The summary of LET, y_F ,the relative value of y_F between different site sizes irradiated by 1000MeV/n particles. The y_F of 2.5 μm site was taken as 100%. (Wang 2006)

Particles	LET	Site Size	2.5 μm	0.5 μm	0.1 μm
$^{56}Fe^{26+}$	149	y_F	139	68.4	18.5
		Ratio	100%	49.2%	13.3%
$^{28}Si^{14+}$	43.3	y_F	40.5	23.2	8.96
		Ratio	100%	57.3%	22.1%
$^{16}O^{8+}$	14.1	y_F	13.7	9.14	4.75
		Ratio	100%	66.7%	34.7%
$^{4}He^{2+}$	0.884	y_F	0.980	0.883	0.779
		Ratio	100%	90.1%	79.5%
Proton	0.221	y_F	0.286	0.289	0.229
		Ratio	100%	101%	80.1%

Table 4.9 is the summary of LET, y_F ,the relative value of y_F between different site sizes irradiated by 1000MeV/n particles for solid-walled detectors. The y_F of 2.5 μm site was taken as 100%. In contrast to the small, nearly constant y_F values in 2.5 μm grid-walled sites which is about 4.5 KeV/μm for all the particles with Z>6, the y_F for the

solid-walled sites is much larger and close to the LET of the incident particles. Lineal energy is approximately equal to LET only for $^{4}He^{2+}$ particles and protons for grid-walled detectors while it is consistent for all the particles simulated for solid-walled detectors of 2.5 μm site diameter. It is because the largest size site has the smallest average number of δ-ray events per primary events. The primary particles contribute most to the y_F. Fig. 4.27 shows the relationship between the charge and the y_F for each site size. Since most of the events in 2.5 μm site are the primary events, its y_F is most likely to be proportional to Z^2 just as LET is. In smaller sites, the contribution of δ-rays increases, so the results will deviate from the Z^2 relationship. The fitting curve shows this tendency.

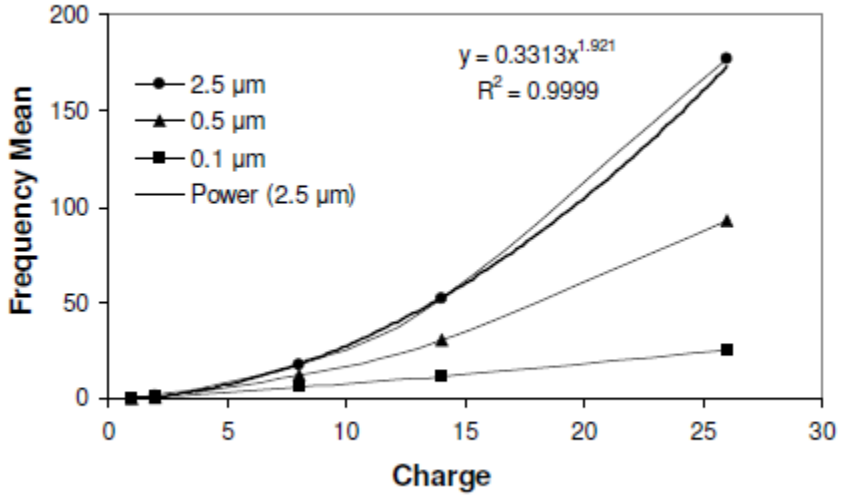

Figure 4.27. The relationship between charge and y_F for each site irradiated by 500 MeV/n particles. The dark line and equation is the fitting curve for 2.5 μm site size. The power of the fitting equation is close to 2. (Wang 2006)

Fig. 4.28 shows the consistency of the size effect for solid-walled detectors. By comparison with Fig. 4.19, we can see that the size effect is more pronounced for the solid-walled detectors than the grid-walled detectors when the systems are irradiated by the same particles with the same energy. This is also caused by the geometry of solid-walled detectors. As we have mentioned above, the fraction of δ-ray events is determined by the ratio of cross-section areas of the wall and the cavity. For the simulated site size of 2.5, 0.5 and 0.1μm, the detector diameters are 31.75, 6.35 and 1.27 mm (1.25, 0.25 and 0.05 inch), respectively. The ratio of cross-section areas of the wall and the cavity is 0.129, 0.729 and 5.63 for 2.5, 0.5 and 0.1 μm site size, respectively. It implies that the average number of δ-ray events per primary events in the 0.1 μm site size is roughly 40 times larger than that of 2.5 μm site size. This value is much larger than the ratio of the average numbers of δ-ray events per primary events in these two different site sizes for grid-walled detectors. This explains that why the size effect is much more pronounced in solid-walled detector systems.

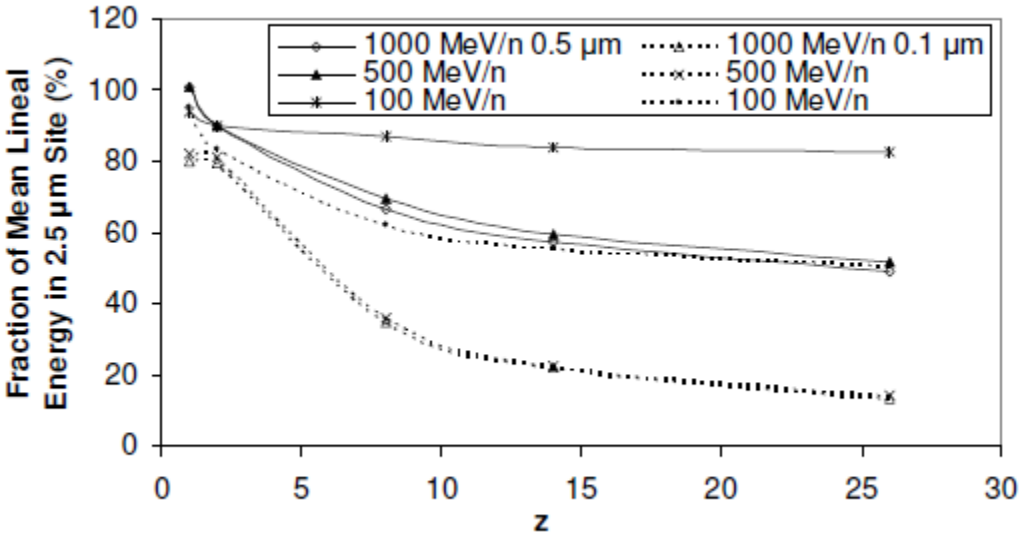

Figure 4.28. Size effect of particles of different Z in 0.5 and 0.1 µm site. The energy used was 1000 MeV/n, 500 MeV/n and 100 MeV/n. The ordinate is the relative value of y_F, with y_F of 2.5 µm site as the denominator. The abscissa is the charge of the primary particles. The particles involved are hydrogen, helium, oxygen, silicon and iron, from left to right. (Wang 2006)

On the other hand, for the solid-walled detectors, the size effect for the particles with higher energy is more distinct than that of the particles with lower energy. The relationship is opposite for the grid-walled detectors. It is because the size effect is also determined by the total number of δ-ray events that deposit energy in the site. Although the particles with lower energy generate more δ-ray than high energy ones, the number of δ-ray events recorded by the detectors is less because the thickness of wall that is within δ-ray range of the detector is smaller. It causes the different tendency of size effect as the change of the particle energy.

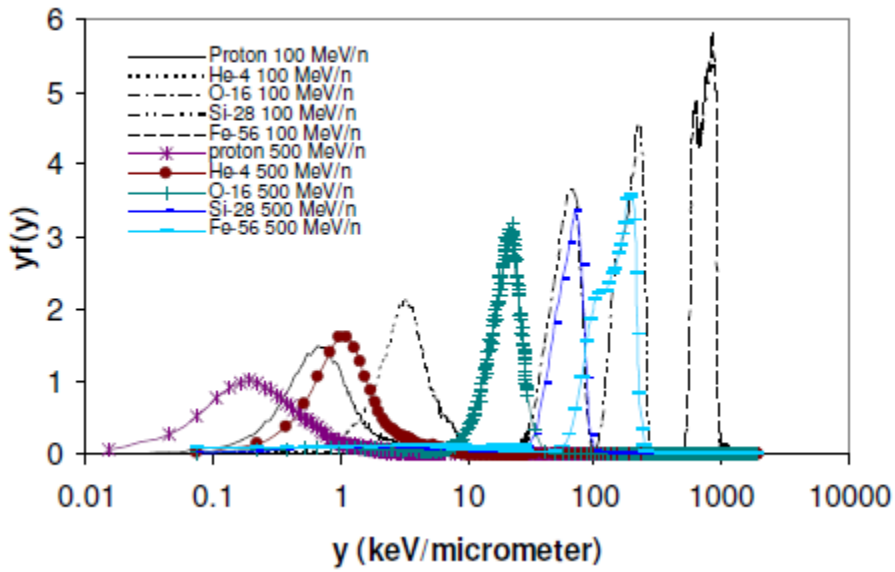

Figure 4.29. The frequency distribution, *yf*(*y*), of 100 and 500 MeV/nucleon ions irradiating solid-walled detectors simulating sites 2.5 μm in diameter. (Wang 2006)

Solid-walled detectors have more distinct size effect than grid-walled ones and different response for particles with different charge and velocity. This makes solid-walled detectors more capable of characterizing mono-energetic HZE particles with different charge. However, if the solid-walled detector system is used in the space radiation environment, it makes the evaluation of the radiation spectrum much more complicated. The collection of distributions in 2.5 μm diameter site for solid-walled detectors was shown in Fig. 4.29. Because each particle shown in the figure has its own mean lineal energy, it's very hard to calculate the fraction of particles of each velocity from the mean lineal energy of the total distribution. Although the different size effect for different particles may give more information from the variance of the mean lineal

energy for sites with different sizes, the approach is much more complicated than that of the grid-walled detector system.

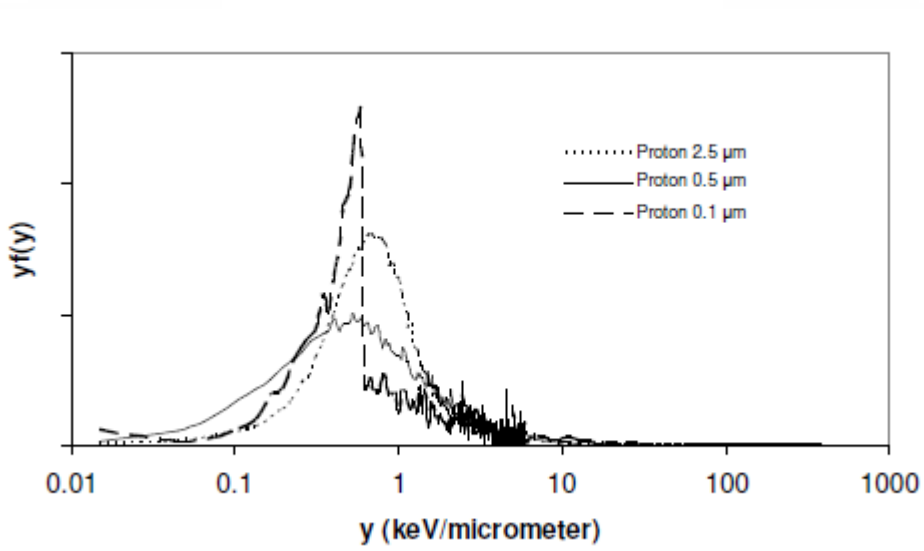

Figure 4.30. The frequency distribution, *yf*(*y*), for a uniform broad beam of 100 MeV/nucleon protons irradiating solid-walled detectors simulating sites 2.5, 0.5, and 0.1 µm in diameter. (Wang 2006)

Furthermore, all our methods are based on the need to distinguish the proton events which consist of 90% of the fluence in galactic cosmic rays. However, the simulation of 100 MeV/n proton shows a broad lineal energy distribution in sites larger than 0.1 µm in diameter (Fig. 4.30), which is partially caused by the electron scattering or wall effect. It is very hard to separate the protons events from the δ-ray events produced by other HZE particles. We have reason to doubt the practicability of solid-walled detector system to characterize the HZE particles in typical space radiation.

CHAPTER V

CONCLUSIONS

This study is a Monte-Carlo simulation of a multiple-size, grid-walled (wall-less) detector system used for microdosimetry of space radiation. Size effects for a series of grid-walled detectors were calculated for HZE particles as well as helium and hydrogen ions. Following the previous attempt at simulations of solid-walled detectors (Wang 2006), this study showed again that the Geant4 toolkit is capable of simulating interaction of materials and HZE particles for cosmic radiation microdosimetry. The Geant4 toolkit can also simulate a mixed radiation field including all the interaction related to cosmic ray dosimetry.

Although a series of approximations were employed in the Geant4 Monte-Carlo toolkit, the simulation results still have remarkable sensitivity to show the size effect for the grid-walled detector systems. This means we can use similar physics processes and data libraries for study in the future without having great impact on data accuracy. All these approximation parameters can be improved to obtain results with better accuracy when more calculation power is available.

Further experimental measurement is necessary to study the performance of such a detector system in an HZE particle field. Comparison of the simulation results and the experimental results is helpful to evaluate the size effect and accuracy of the simulations. The skills of normalization, start point treatment and spectrum welding can be used in

experiments. The techniques of data analysis for simulations can also be applied in experimental data analysis.

The simulated site sizes chosen were 2.5, 0.5 and 0.1 μm for this study and for the study for solid-walled detectors. The results show that such a group of site sizes demonstrates the size effect for various particles in a wide energy range. Although the solid-walled detector system demonstrates a more distinct size effect with the same group of sizes than the grid-walled one, the variance of individual response of the solid-walled detector system for particles with the same velocity but different charge (mass) brings more complication to characterize the velocity of incident particles. Furthermore, the unique spectral characteristics of protons restrict the practicability of a solid-walled detector system in the space radiation environment.

The ability of the detector system to characterize HZE radiations is proved. The characterizing ability is consistent for particles with different mass and energy. By analyzing the spectra from the three detectors, we can easily achieve a practical evaluation of radiation spectrum by determining the fraction of HZE particles in 4 different energy (velocity) bins and distinguish particles with similar LET. Further simulations of particles with more variety of mass and energy are necessary to study the characterizing ability in the uniform complex cosmic ray field. The idea of using the size effect to characterize HZE particles for better estimation of effective dose is shown to be feasible. This encourages the construction of such a detector system.

However, the Geant4 simulations also suggested that there were a few technical problems when constructing this system. The calculations showed that the ratio of

physical detector diameters should be made as large as possible to manifest the size effect, but the larger the ratio of diameters, the more small detectors will be needed, and the more complex the construction and electronics will become. Another problem is that the size of the vacuum chamber should be large enough to simulate a region of a continuous medium in order to show the effect of the differences in δ-ray range, but the system must be relatively compact and light in weight so that it can be proposed for use in routine measurement of radiation exposure in the space station and space shuttle. The results (Fig. 4.2) suggest that the vacuum chamber diameter would have to simulate 8000 micrometers of unit density material in order to properly represent 95% of the delta ray events. If a 5 cm diameter detector simulates 2.5 micrometers, the vacuum chamber would have to be 160 meters in diameter to simulate the 8000 micrometer diameter tissue volume. The third problem is that the relatively high δ-ray event count rates in the spectra might introduce significant event losses due to signal pileup and dead time in the system. These problems need to be solved in the future before making a practical design of this detector system.

REFERENCES

Agostinelli, S.; Allison, J.; Amako, K.; Apostolakis, J.; Araujo, H.; Arce, P.; Asai, M.; Axen, D.; Banerjee, S.; Barrand, G.; Behner, F.; Bellagamba, L.; Boudreau, J.; Broglia, L.; Brunengo, A.; Burkhardt, H.; Chauvie, S.; Chuma, J.; Chytracek, R.; Cooperman, G.; Cosmo, G.; Degtyarenko, P.; Dell'Acqua, A.; Depaola, G.; Dietrich, D.; Enami, R.; Feliciello, A.; Ferguson, C.; Fesefeldt, H.; Folger, G.; Foppiano, F.; Forti, A.; Garelli, S.; Giani, S.; Giannitrapani, R.; Gibin, D.; Gomez Cadenas, J.J.; Gonzalez, I.; Gracia Abril, G.; Greeniaus, G.; Greiner, W.; Grichine, V.; Grossheim, A.; Guatelli, S.; Gumplinger, P.; Hamatsu, R.; Hashimoto, K.; Hasui, H.; Heikkinen, A.; Howard, A.; Ivanchenko, V.; Johnson, A.; Jones, F.W.; Kallenbach, J.; Kanaya, N.; Kawabata, M.; Kawabata, Y.; Kawaguti, M.; Kelner, S.; Kent, P.; Kimura, A.; Kodama, T.; Kokoulin, R.; Kossov, M.; Kurashige, H.; Lamanna, E.; Lampen, T.; Lara, V.; Lefebure, V.; Lei, F.; Liendl, M.; Lockman, W.; Longo, F.; Magni, S.; Maire, M.; Medernach, E.; Minamimoto, K.; Mora de Freitas, P.; Morita, Y.; Murakami, K.; Nagamatu, M.; Nartallo, R.; Nieminen, P.; Nishimura, T.; Ohtsubo, K.; Okamura, M.; O'Neale, S.; Oohata, Y.; Paech, K.; Perl, J.; Pfeiffer, A.; Pia, M.G.; Ranjard, F.; Rybin, A.; Sadilov, S.; Di Salvo, E.; Santin, G.; Sasaki, T.; Savvas, N.; Sawada, Y.; Scherer, S.; Sei, S.; Sirotenko, V.; Smith, D.; Starkov, N.; Stoecker, H.; Sulkimo, J.; Takahata, M.; Tanaka, S.; Tcherniaev, E.; Safai Tehrani, E.; Tropeano, M.; Truscott, P.; Uno, H.; Urban, L.; Urban, P.; Verderi, M.;

Walkden, A.; Wander, W.; Weber, H.; Wellisch, J.P.; Wenaus, T.; Williams, D.C.; Wright, D.; Yamada, T.; Yoshida, H.; Zschiesche, D. Geant4 – a simulation toolkit. *Nucl. Instrum. Meth.* A. 506: 250–303; 2003.

Allison, J.; Amako, K.; Apostolakis, J.; Araujo, H.A.A.H.; Arce Dubois, P.A.A.D.P.; Asai, M.A.A.M.; Barrand, G.A.B.G.; Capra, R.A.C.R.; Chauvie, S.A.C.S.; Chytracek, R.A.C.R.; Cirrone, G.A.P.A.C.G.A.P.; Cooperman, G.A.C.G.; Cosmo, G.A.C.G.; Cuttone, G.A.C.G.; Daquino, G.G.A.D.G.G.; Donszelmann, M.A.D.M.; Dressel, M.A.D.M.; Folger, G.A.F.G.; Foppiano, F.A.F.F.; Generowicz, J.A.G.J.; Grichine, V.A.G.V.; Guatelli, S.A.G.S.; Gumplinger, P.A.G.P.; Heikkinen, A.A.H.A.; Hrivnacova, I.A.H.I.; Howard, A.A.H.A.; Incerti, S.A.I.S.; Ivanchenko, V.A.I.V.; Johnson, T.A.J.T.; Jones, F.A.J.F.; Koi, T.A.K.T.; Kokoulin, R.A.K.R.; Kossov, M.A.K.M.; Kurashige, H.A.K.H.; Lara, V.A.L.V.; Larsson, S.A.L.S.; Lei, F.A.L.F.; Link, O.A.L.O.; Longo, F.A.L.F.; Maire, M.A.M.M.; Mantero, A.A.M.A.; Mascialino, B.A.M.B.; McLaren, I.A.M.I.; Mendez Lorenzo, P.A.M.L.P.; Minamimoto, K.A.M.K.; Murakami, K.A.M.K.; Nieminen, P.A.N.P.; Pandola, L.A.P.L.; Parlati, S.A.P.S.; Peralta, L.A.P.L.; Perl, J.A.P.J.; Pfeiffer, A.A.P.A.; Pia, M.G.A.P.M.G.; Ribon, A.A.R.A.; Rodrigues, P.A.R.P.; Russo, G.A.R.G.; Sadilov, S.A.S.S.; Santin, G.A.S.G.; Sasaki, T.A.S.T.; Smith, D.A.S.D.; Starkov, N.A.S.N.; Tanaka, S.A.T.S.; Tcherniaev, E.A.T.E.; Tome, B.A.T.B.; Trindade, A.A.T.A.; Truscott, P.A.T.P.; Urban, L.A.U.L.; Verderi, M.A.V.M.; Walkden, A.A.W.A.; Wellisch, J.P.A.W.J.P.; Williams, D.C.A.W.D.C.; Wright, D.A.W.D.; Yoshida, H.A.Y.H.

Geant4 developments and applications. *IEEE Trans. Nucl. Sci.* 53: 270–278; 2006.

Badhwar, G.D. Shuttle radiation dose measurements in the international space station orbits. *Radiat. Res.* 157: 69–75; 2002.

Brooks, A.L.; Bao, S.; Rithidech, K.; Couch, L.A.; Braby, L.A. Relative effectiveness of HZE iron-56 particles for the introduction of cytogenetic damage in vivo. *Radiat. Res.* 155: 353-359; 2001.

Chatterjee, A.; Schefer, H.J. Microdosimetric structure of heavy ion tracks in tisure. *Radiat. Environ. Biophys.* 13: 215-227; 1976.

Cougnet, C.; Crosby, N. B.; Foullon, C.; Heynderickx, D.; Eckersley, S.; Guarnieri, V.; Lobascio, C.; Masiello, S.; Parodi, P.; Perino, M.A.; Rampini, R.; Guatelli, S.; Pia, M.G.; Holmes-Siedle, A.; Nieminen, P.; Parisi, G.; Tamburini, V.; Spillantini, P.; Tracino, E. Radiation exposure and mission strategies for interplanetary manned missions (REMSIM). *Earth Moon Planets* 94: 279–285; 2004.

Guetersloh, S.B.; Borak, T.B.; Taddei, P.J.; Zeitlin, C.; Heilbronn, L.; Miller, J.; Murakami, T.; Iwata, Y. The response of a spherical tissue-equivalent proportional counter to defferent ions having similar linear energy transfer. *Radiat. Res.* 161: 64-71; 2004.

Howard, A.S.; Araujo, H. Simulation and analysis for astroparticle experiments. *Nucl. Phys. B-Proc. Sup.* 125: 320–326; 2003.

ICRP. International Commission of Radiation on Radiological Protection. Recommendations of the International Commission on Radiological Protection (ICRP Publication 60, Annals of the ICRP, Vol. 21, No. 1-3). New York, U.S.A.: Pergamon Press; 1990.

ICRU. International Commission on Radiation Units and Measurements. Stopping powers and ranges for protons and alpha particles. Report 49. Bethesda, MD; 1993.

Kellerer, A.M. An assessment of wall effects in microdosimetric measurements. *Radiat. Res.* 47: 377; 1971.

Kliauga, P. Measurement of single-event energy deposition spectra at 5 nm to 250 nm simulated site sizes. *Radiat. Prot. Dosim.* 31, 119-123; 1990.

Kliauga, P.; Waker, A. J.; Barth, J. Design of tissure-equivalent proportional counters, *Radiat. Prot. Dosim.* 61: 309-322; 1995.

Metting, N.F.; Rossi, H.H.; Braby, L.A. Microdosimetry near the Trajectory of High-Energy Heavy ions. *Radiat. Res.* 116: 183-195; 1988.

NCRP. National Council on Radiation Protectoion and Measurements. Guidance on Radiation Received in Space Activities (NCRP 98). Bethesda, MD, USA: NCRP; 1989.

Rossi, H.H.; Rosenzweig, W. A device for the measurement of dose as a function of specific ionization. *Radiology* 64: 404–411; 1955.

Rossi, H.H.; Zaider M. Microdosimetry and Its Applications. Springer-Verlag, Berlin; 1996.

Wang, X.; Liu, H.; Xia, Z.; Braby, L.A. Lineal Energy as a Function of Site Size for HZE Radiation. *Radiat. Prot. Dosim.* 122: 367-368; 2004.

Wang, X. Monte Carlo Simulations of Solid Walled Proportional Counters with Different Site Size for HZE Radiation. MSc thesis, Department of Nuclear Engineering, Texas A&M University; 2006.

Zhang, C.; Dunn, D.E.; Katz, R. Radial distribution of dose and cross sections for the inactivation of dry enzymes and viruses. *Radiat. Prot. Dosim.* 13: 215-218; 1985.

APPENDIX

Calculation for the mixed spectrum

The number of δ-ray events per primary event N_δ for particles with different energies can be found in table 4.1 to 4.6. In the mixed radiation field, it means a number of N_δ δ-rays events will be recorded for each primary event. This means the total number of events recorded in the detector will be proportional to $1 + N_\delta$ for each nuclide when the number of each ion particles is the same. Thus, we can use $1 + N_\delta$ as the weighting factor to calculate the mean lineal energy for a mixed field. Considering a mixed ion beam consisting of 90% protons, 2% $^{4}He^{2+}$, 2% $^{12}C^{6+}$, 2% $^{16}O^{8+}$, 2% $^{28}Si^{14+}$, and 2% $^{56}Fe^{26+}$, if we removed the events produced by protons from the spectrum, the mean lineal energy for particles besides protons with energy of 1000 MeV/n in a 0.1 μm site would be

$$\begin{aligned} y_{F,1000} = {} & [2\%*(1+N_{\delta(He,1000)})*y_{F(He,1000)}+2\%*(1+N_{\delta(C,1000)})*y_{F(C,1000)}+2\%*(1+N_{\delta(O,1000)}) \\ & *y_{F(O,1000)}+2\%*(1+N_{\delta(Si,1000)})*y_{F(Si,1000)}+2\%*(1+N_{\delta(Fe,1000)})*y_{F(Fe,1000)}] / \\ & [2\%*(1+N_{\delta(He,1000)})+2\%*(1+N_{\delta(C,1000)})+2\%*(1+N_{\delta(O,1000)})+2\%*(1+N_{\delta(Si,1000)}) \\ & +2\%*(1+N_{\delta(Fe,1000)})] \\ = {} & 3.411 \text{ KeV/μm} \end{aligned}$$

The weighting factor for 1000 MeV/n ions other than protons, for calculation of the total mean lineal energy of the mixed spectrum, would be

$$\begin{aligned} w_{1000} = {} & 2\%*(1+N_{\delta(He,1000)})+2\%*(1+N_{\delta(C,1000)})+2\%*(1+N_{\delta(O,1000)})+2\%*(1+N_{\delta(Si,1000)}) \\ & +2\%*(1+N_{\delta(Fe,1000)}) \\ = {} & 74.98 \end{aligned}$$

Use the same method for the 100 MeV/n particles besides protons, the mean lineal energy and the weighting factor would be

$$\begin{aligned} y_{F,100} = {} & [2\%*(1+N_{\delta(He,100)})*y_{F(He,100)}+2\%*(1+N_{\delta(C,100)})*y_{F(C,100)}+2\%*(1+N_{\delta(O,100)}) \\ & *y_{F(O,100)}+2\%*(1+N_{\delta(Si,100)})*y_{F(Si,100)}+2\%*(1+N_{\delta(Fe,100)})*y_{F(Fe,100)}] / \\ & [2\%*(1+N_{\delta(He,100)})+2\%*(1+N_{\delta(C,100)})+2\%*(1+N_{\delta(O,100)})+2\%*(1+N_{\delta(Si,100)}) \\ & +2\%*(1+N_{\delta(Fe,100)})] \\ = {} & 3.835 \text{ KeV/μm} \end{aligned}$$

$$\begin{aligned} w_{100} = {} & 2\%*(1+N_{\delta(He,100)})+2\%*(1+N_{\delta(C,100)})+2\%*(1+N_{\delta(O,100)})+2\%*(1+N_{\delta(Si,100)}) \\ & +2\%*(1+N_{\delta(Fe/100)}) \\ = {} & 200.59 \end{aligned}$$

From the lineal energy distribution of the total spectrum (70% 1000 MeV/n and 30% 100 MeV/n) besides protons shown in Fig. 4.23, the total mean lineal energy is y_{total} = 3.652 KeV/μm.

Assume the fraction of 1000 MeV/n ions is x, then the fraction of 100 MeV/n ions would be 1-x. Thus,

$$y_{total} = [y_{F,1000} * w_{1000} * x + y_{F,100}\ w_{100} * (1-x)] / [w_{1000} * x + w_{100} * (1-x)]$$
$$= [3.411\text{KeV/μm} * 74.98 * x + 3.835\text{KeV/μm} * 200.59 * (1-x)] / [74.98 * x + 200.59 * (1-x)]$$
$$= 3.652\ \text{KeV/μm}$$

Solve this equation and we can get the fraction of 1000 MeV/n ions is 67% and the fraction of 100 MeV/n ions is 33%.

VITA

Name:	Haifeng Liu
Address:	Nuclear Engineering Dept, Texas A&M University, 3133 TAMU, College Station, 77843-3133
Email Address:	liuhf@tamu.edu
Education:	B.S., Engineering Physics, Tsinghua University, Beijing, China, 1999 M.S., Engineering Physics, Tsinghua University, Beijing, China, 2003 Ph.D., Health Physics, Texas A&M University, College Station, Texas, USA, 2012